Title

Searching for High-Performance Magnesium Cathodes using High-Throughput Computational Methods

Permalink

https://escholarship.org/uc/item/03z851z1

Author

Rutt, Ann Catherine

Publication Date

2023

Peer reviewed|Thesis/dissertation

Searching for High-Performance Magnesium Cathodes
using High-Throughput Computational Methods

By

Ann Rutt

A dissertation submitted in partial satisfaction of the

requirements for the degree of

Doctor of Philosophy

in

Engineering - Materials Science and Engineering

in the

Graduate Division

of the

University of California, Berkeley

Committee in charge:

Professor Kristin A. Persson, Chair
Professor Gerbrand Ceder
Professor Bryan McCloskey

Summer 2023

Searching for High-Performance Magnesium Cathodes
using High-Throughput Computational Methods

Abstract

Searching for High-Performance Magnesium Cathodes
using High-Throughput Computational Methods

by

Ann Rutt

Doctor of Philosophy in Engineering - Materials Science and Engineering

University of California, Berkeley

Professor Kristin A. Persson, Chair

There is an increasing need for sustainable energy storage solutions as fossil fuels are replaced by renewable energy sources. Multivalent batteries, and specifically Mg batteries, are one energy storage technology that researchers continue to develop with hopes to surpass the performance of Li-ion batteries. However, the limited energy density and transport properties of Mg cathodes remain as critical challenges preventing the realization of high-performance multivalent batteries. While spinel $Mg_xTi_2S_4$ and layered Mg_xTiS_2 represented significant advancements in Mg cathodes, with improved gravimetric capacities compared to the original prototype Mg cathode, Chevrel $Mg_xMo_6S_8$, their performance is limited by their low voltages and poor solid-state ionic mobility. The absence of high-performance Mg cathodes motivates the need to develop new materials discovery approaches and expand material design strategies to improve multivalent ion solid-state mobility and further advance multivalent batteries.

A computational screening approach to identify high-performance multivalent intercalation cathodes among materials that do not contain the working ion of interest has been developed, which greatly expands the search space that can be considered for materials discovery. This approach has been applied to magnesium cathodes as a proof of concept and four resulting candidate materials are discussed in further detail: NASICON $V_2(PO_4)_3$, birnessite $NaMn_4O_8$, tavorite $MnPO_4F$, and spinel MnO_2. This methodology includes the automated evaluation of solid-state mobility in high-throughput which enables filtering candidate cathode materials by their intrinsic transport properties such as tavorite $MnPO_4F$ and spinel MnO_2, where high migration barriers were predicted. In examining the ion migration environment and associated Mg^{2+} migration energy in these four materials, local energy maxima are found to correspond with pathway positions of lower coordination where Mg^{2+} passes through a plane of anion atoms. While previous works have established the influence of local coordination on multivalent ion mobility, these results suggest that considering both the type of local bonding

environment as well as the available free volume for the mobile ion along its migration pathway can be significant for improving solid-state mobility.

Two novel Mg cathode candidates were identified from the preliminary results in developing this novel computational screening approach: ε-VOPO$_4$ and zircon EuCrO$_4$. These materials were experimentally pursued to characterize their electrochemical properties and evaluate their viability as Mg cathodes. While Mg intercalation was experimentally verified in ε-VOPO$_4$ and three zircon materials (YVO$_4$, EuVO$_4$, and EuCrO$_4$), the measured gravimetric capacities were notably lower than expected. The properties of these materials from this initial experimental work are not yet sufficient to serve as high-performance Mg cathodes.

The computational investigation of ABO$_4$ zircon materials (A = Y, Eu and B = V, Cr) as Mg intercalation cathodes identified remarkably good Mg-ion transport properties (migration barriers <250 meV) across multiple chemistries in this structural family. These properties were attributed to their unique structural motif of overlapping polyhedra along the diffusion pathway in zircons which appears instrumental for promoting good Mg-ion mobility. This motif results in a favorable "6-5-4" change in coordination that avoids unfavorable sites with lower coordination along the diffusion pathway. Diffusion pathways composed of polyhedra with overlapping volumes offers a promising new structural design metric for future Mg cathode development.

The introduced novel cathode computational screening approach is a significant advancement in expanding the diversity of materials considered for materials discovery and accounting for intrinsic solid-state mobility properties. Additional investigations into ε-VOPO$_4$ and ABO$_4$ zircons as Mg intercalation cathodes illustrate the value of this approach in identifying novel cathode materials. However further study and optimization will be required to overcome the limited experimental electrochemical performance in these materials. This highlights limitations in the introduced screening methodology which only considers phase stability, energy density properties, and transport properties intrinsic to the host crystal structure at the Angstrom scale. Despite its limitations, further study of materials evaluated by this screening approach yielded valuable insights into strategies for improving multivalent ion transport. Building upon these findings, such as the role of site volume and overlapping polyhedra along the diffusion pathway, may inform further advancements in promoting multivalent ion transport and the discovery of high-performance Mg cathodes.

For any brave souls who work in the multivalent battery research.

Especially, the intrepid experimentalists and their admirable perseverance.

Table of Contents

Acknowledgements

The end of my time in graduate school was unexpectedly difficult. In my acknowledgements, I wanted to focus on the smaller moments of kindness where I found support amid my challenging circumstances. The cumulative effect of little things can have a big impact. As I look back on this period, I hope that these comforting actions and moments will wash over the negative parts.

Thank you to my friends with our regular touch points that helped me stay connected and grounded throughout graduate school: coffee with Matt McDermott and Jordan Burns, Asha Teahouse with Emma Vargo, and watching *Farmer Needs a Wife* with Nathan Szymanski.

I loved meeting with the members of my anti-racism reading group: Nivedina Sarma, Jesse Schimpf, Tofunmi Ogunfunmi, Erin Katz, Anna Weldy, Alhad Deshpande, and Isaac Joyner. Our lunch meetings were a consistent and caring space that were always a highlight to my week.

A very big thank you to Emma Vargo, Michael Janner, and Becky Hanscam for kindly opening up their apartments to me for temporary housing when I didn't have a place to stay after my apartment flooded.

Thank you to Jordan Burns, Howard Li, and Matt Horton for going on a walk with me to help me calm down after I was crying from an upsetting meeting. I'm also grateful to Ryan Kingsbury and Rishabh Guha for reaching out with care afterwards and reaffirming my past contributions.

The times when others asked how I was and kindly listened over lunch time or when we ran into each other on the LBL shuttle or hallways at work were also helpful. It was always a pleasure to cross paths with Guy Moore on the LBL shuttle and once he very kindly gave me a hug and asked if there were any ways he could support me. Alex Epstein consistently made time to check-in if we bumped into each other in the kitchen. I also wanted to note one smaller group lunch I enjoyed with Orion Cohen and Bryant Li.

Thank you to Jiyoon Kim for sending me a goofy picture of her horse, Reve, that made me smile when I was feeling down. Mackinzie Farnell also helped me feel better by sharing she was sorry about what I was experiencing. I find hope and optimism in the younger graduate students who pick up the baton.

Qian Chen was also a wonderful colleague who went out of her way to identify how she could help me complete my work when I was feeling overextended.

Thank you to Reed Yalisove, Luis Rangel DeCosta, and Tanzil Chowdhury for advocating for me. I appreciated the sincere gesture when Luis bought me coffee at MY Coffee Roastery.

I was also touched by the times others showed their support with homemade food. I fondly recall one delicious batch of lentil soup from Hetal Patel that was too sweet for her. Humberto Batize Guerroero offered his copyediting services to help me graduate over pozole soup that was prepared with Ana. Opening your home to share a cozy meal with others is always a treat.

I'm also very fortunate for everyone who happened to be in the right place at the right time and made time for me when I needed support. Thank you to Max Gallant for sharing his table with me when I was crying and hyperventilating after an upsetting meeting. I'm also very grateful for one difficult morning at work where Jordan Burns, Oxana Andruic, and Hetal Patel talked with me and offered hugs afterwards. Thank you to Matt McDermott for comforting me when I had a difficult time before my last group meeting presentation.

Thank you to Rachel Clune, my housemate, for always being open to listen and offering her reassuring perspective when we were at home. And for offering her office space when I needed additional motivation to work on my thesis towards the end.

This is inevitability an imperfect and incomplete account primarily based upon the period when I was actively working on my thesis. For the additional moments and people unmentioned throughout my graduate school journey, I am also grateful, and I hope that I have expressed my appreciation for your support in other ways.

1. Introduction[1]

1.1. Motivating research in Mg batteries as a "Beyond Li-ion" energy storage technology

Multivalent batteries are one of several emerging "beyond Li-ion" battery energy storage technologies that aim to enable large-scale renewable energy [1–4]. While Li-ion batteries are already being adopted in fully electric vehicles, the widespread displacement of fossil fuels requires further reductions to cost and increased energy densities of automotive batteries [5]. Manufacturing improvements have significantly reduced the cost of Li-ion battery modules to less than $200/kWh today, but prices must further drop to $100/kWh to reach parity with gasoline cars [6]. Current Li-ion batteries also fall short of the 350 Wh/kg and 750 Wh/L cell level energy density targets in order to achieve a 300 mile driving range for an electric vehicle, which were set by the U.S. Department of Energy and U.S. Advanced Battery Consortium [5]. While further development is needed, improving multivalent batteries offers an avenue to surpass the performance of Li-ion batteries and meet the needs of more demanding energy storage applications, such as electric vehicles.

Although it is difficult to compete with the gravimetric energy density of lithium active materials, as lithium is one of the lightest elements in the periodic table, multivalent chemistries have an advantage with respect to volumetric energy density. Each multivalent ion carries multiple charges (M^{n+} where n > 1), yielding larger capacity when the same number of working ions is stored in a given electrode volume compared with monovalent ions (M^{1+}) such as lithium. The core promise of higher energy density with multivalent batteries is tied to the possibility of utilizing multivalent metal anodes. Whereas conventional Li-ion batteries generally adopt lower energy density graphite anodes to avoid cell shorting caused by the dendritic growth of lithium metal, multivalent metals are less prone to dendrite formation. Thus, metal anodes can be used in multivalent batteries and avoid this compromise between energy density and safety. While multivalent batteries with metal anodes are attractive as a high volumetric energy density alternative to Li-ion batteries, research to establish practical battery chemistries that realize the full theoretical potential of multivalent batteries is ongoing.

Of the multivalent battery chemistries (Mg^{2+}, Ca^{2+}, Zn^{2+}, Al^{3+}, etc.), the most progress has been made with magnesium batteries since the first lab scale prototype magnesium cell was reported in 2000 [7,8]. However, wider adoption of magnesium batteries has been restricted by their limited performance due to the properties of available Mg intercalation cathodes. Research efforts in Mg cathodes focus on identifying materials with improved energy density and rate capability properties for high-performance batteries. To provide a quantitative estimate, one cell-level analysis outlined cathode active material properties of 3.1 V (vs. Mg/Mg^{2+}) and 165 mAh/g as a possible combination that would approach the 750 Wh/L cell level volumetric energy density target for electric vehicles [5]. For sufficient working ion solid-state mobility to permit C/2 battery cycling rate capability at room temperature, it has also been estimated that the migration barriers must be below 525 meV for micron-sized or below 650 meV for nano-sized active material particles [9]. While progress has been made, the best available Mg cathodes still exhibit inferior voltages compared to state-of-the-art Li-ion cathodes, and poor solid-state

---

[1] Portions of this chapter are adapted from References [5,10,114].

mobility, which results in insufficient rate capability [10]. The identification of high-performance Mg cathodes is an issue that must be overcome in order to realize a Mg battery chemistry that can outperform Li-ion batteries and warrant commercialization [4,5,8].

1.2. Advancements in Mg cathodes still fall short of performance targets

There have been a number of extensive reviews already written on Mg cathodes [5,8,11], so the discussion here is limited and only highlights a few select Mg intercalation cathode materials. Each of these Mg cathodes has experimental evidence demonstrating reversible Mg intercalation and repeated cycling in full cells using magnesium metal anodes and non-aqueous liquid organic electrolytes. In summary, spinel $Mg_xTi_2S_4$ [12,13] and layered Mg_xTiS_2 [12,14], which were both reported in 2016, represent the most promising advancements in Mg cathodes compared to the original Mg cathode, Chevrel $Mg_xMo_6S_8$ [15]. Quantitative metrics for energy density and solid-state mobility are summarized in Table 1. Both materials show improved capacities compared to 100 mAh/g for Chevrel $Mg_xMo_6S_8$ and begin to approach the previously established target of 165 mAh/g for electric vehicles [5]. However, both the spinel $Mg_xTi_2S_4$ and the layered Mg_xTiS_2 cathodes share two limitations that must be overcome in order to realize high-performance magnesium batteries: 1) low voltages (1.2 V vs. Mg/Mg^{2+} vs. the 3.1 V target [5]) and 2) poor solid-state mobility (requiring elevated cycling temperatures of 60°C and corresponding higher Mg^{2+} migration barriers) [10].

System	Cell Voltage (V)	Specific Capacity (mAh/g)	Fraction of Theoretical Capacity (%)	Migration Barrier (meV)
Commercialized Li-ion Cathodes [16]	~3.4-4.1	~140-300	55-97%	~200-550
Chevrel $Mg_xMo_6S_8$ [15,17]	1.1	100 (C/8 rate, 25°C)	78%	270
Layered Mg_xTiS_2 [12,14]	1.2	140 (C/10 rate, 60°C)	48%	1160
Spinel $Mg_xTi_2S_4$ [13,18]	1.2	160 (C/10 rate, 60°C)	79%	550-615
Mg Cathode Electric Vehicle Target [5,19]	3.1	165 (25°C)	100%	< 525-650

Table 1. A comparison of experimental energy density and theoretical transport properties of current available Mg cathodes with Li-ion cathodes and the targeted performance for electric vehicles. While from a capacity standpoint, current available Mg cathodes are close to the 165 mAh/g target, their voltages are much lower than the 3.1 V target at 1.1-1.2 V. Notably, while the capacities of layered Mg_xTiS_2 and spinel $Mg_xTi_2S_4$ are improved compared to Chevrel $Mg_xMo_6S_8$, their migration barriers are much higher and require elevated testing temperature of 60°C.

Chevrel $Mg_xMo_6S_8$ and $Mg_xMo_6S_6Se_2$. The Chevrel phase ($Mg_xMo_6T_8$, where T = S, Se, or their combination), which consists of a Mo_6 octahedral cluster inside a T_8 cube, was the first prototype Mg cathode for room temperature cycling with a theoretical capacity of 129 mAh/g at 1.1V [20,21]. The first functional Mg metal battery used a Chevrel $Mg_xMo_6S_8$ (0 < x < 2) cathode [20] but only 75-80% of the Mg could be extracted which was attributed to the limited Mg mobility in a fraction of the working ion sites resulting from the ring-trapping mechanism specific to the Chevrel structure [22]. Theoretical studies showed that substitution of

S with Se increases the lattice size and distorts the geometry of the structure to disrupt the ring-trapping mechanism [23,24]. Further exploration into anion substitution for this material class found slightly improved electrochemical performance in Chevrel $Mg_xMo_6S_6Se_2$ with an initial capacity of 110 mAh/g at 1.1 V vs. Mg/Mg^{2+} and good capacity retention for 100 cycles at room temperature [22]. The computed Mg^{2+} migration barriers in Mo_6Se_8 (180 meV) are lower than in Mo_6S_8 (270 meV) [25] consistent with the better experimental performance of $Mg_xMo_6S_6Se_2$ over that of $Mg_xMo_6S_8$ in Mg cells and observed room temperature cycling of Chevrels [22].

Layered Mg_xTiS_2 and Mg_xTiSe_2. Reversible Mg intercalation has been demonstrated in both layered Mg_xTiS_2 [26] and layered Mg_xTiSe_2 [27] ($0 < x < 0.5$), with average voltages of 1.2 V (TiS_2) and 0.9 V ($TiSe_2$) vs. Mg/Mg^{2+} and gravimetric capacities of 115 mAh/g (TiS_2) and 110 mAh/g ($TiSe_2$). It should also be noted that although 85% of the theoretical capacity for layered $TiSe_2$ (130 mAh/g) could be obtained by cycling at room temperature, only 48% of the theoretical capacity of layered TiS_2 (239 mAh g^{-1}) could be extracted even at 60°C. Good capacity retention was experimentally demonstrated for layered TiS_2 for 40 cycles using a C/10 rate at 60°C [26]. However, layered $TiSe_2$ shows better electrochemical performance at room temperature than layered TiS_2 [11]. These experimental observations are supported by the calculated Mg^{2+} migration barriers of >1060 meV in layered TiS_2 [28,29] and 650 meV for layered $TiSe_2$ [30].

Spinel $Mg_xTi_2S_4$. Multiple spinels ($Mg_xB_2X_4$, where $0 < x < 1$, B is a transition metal, and X = O, S) have been studied as Mg cathodes [18,31]. The best electrochemical performance has been reported for $Mg_xTi_2S_4$ at 60°C with an average voltage of 1.1 V (vs. Mg/Mg^{2+}) and capacity of 190 mAh/g, which approaches 80% of the theoretical value (239 mAh/g) [32,33]. This was achieved with cycling at a rate of C/5 between 0.5–1.8 V while longer term cycling, which was performed at a C/10 rate, demonstrated reversible capacities between 160-140 mAh/g for 40 cycles. Notably, cycling at an elevated temperature of 60°C improved the electrochemical performance of spinel $Mg_xTi_2S_4$ [11] which is consistent with the higher Mg^{2+} migration barrier predicted for spinel Ti_2S_4 between 550-615 meV [32,34].

1.3. Energy density and transport performance trade-off challenges in Mg cathodes

The challenge of identifying multivalent intercalation cathodes with good solid-state mobility correlates directly to their potential for higher capacity [5]. While the higher valence of multivalent ions can lead to a higher energy density, there is also a trade-off associated with poorer transport due to the stronger Coulombic interactions between the mobile multivalent ion and surrounding cathode host lattice. Some strategies to improve multivalent ion transport, such as substituting larger and more polarizable anions in the host material to lower migration barriers (e.g., selenides have better screening properties over sulfides, sulfides have better screening properties over oxides) also result in lower cathode voltages because anions with higher polarizability are also more easily oxidized [5,35]. While numerous factors at various length scales can contribute to poor transport, high migration barriers for multivalent ion transport within the crystal structure at the Angstrom scale must be addressed first.

Although Li-ion cathodes are typically synthesized in the discharged state where lithium is contained in the material, the success of similar strategies for multivalent cathodes have been called into question [19]. Previous work [19] has shown that multivalent ion mobility correlates

with the local coordination topology along the diffusion path, favoring flatter energetic landscapes with no strong binding sites for the multivalent ion. For example, materials which contain Mg in their as-synthesized states tend to exhibit relatively strong Mg binding sites, and hence poorer mobility. In fact, the most successful Mg cathodes have originated from compounds synthesized in a form without Mg. In the case of Chevrel $Mg_xMo_6S_8$, the copper-containing $CuMo_3S_4$ is synthesized and the copper then chemically removed [7]. Similarly, for spinel $Mg_xTi_2S_4$, $CuTi_2S_4$ is synthesized and then the copper removed by oxidation [13]. Layered Mg_xTiS_2 can be synthesized free of any intermediate compound as TiS_2 [14]. A successful Mg cathode which has been synthesized in the discharged state (where the Mg ion is contained in the structure) has yet to be reported [5]. Hence, one may extrapolate that identifying new multivalent cathodes among materials that already contain the multivalent ion of interest would yield scarce results and new materials discovery approaches are needed [10].

1.4. Research goals: searching for high-performance magnesium cathodes

Two research goals were pursued in this dissertation. The first goal is focused on the materials discovery of high-performance Mg cathodes with sufficient energy density and Mg mobility to make Mg batteries competitive for elective vehicles. The second goal is the scientific objective of further refining and expanding material design rules to promote better Mg-ion transport. The second chapter introduces a novel high-throughput computational screening approach which uses density functional theory calculations to assess intercalation cathode material properties. A novel component of this approach is the use of tools that expand evaluation capabilities to materials where the working ion site is not previously known, which allows access to a much more diverse materials search space. Another significant advancement in this approach is including the high-throughput evaluation of intrinsic transport properties for any inorganic crystalline material. This methodology was demonstrated by applying it to search for high-performance Mg cathodes. The subsequent chapters focus on deeper investigations into two new Mg cathode candidates identified with this screening methodology. One promising candidate due to its energy density properties, ε-$VOPO_4$, was experimentally validated and illustrates the value of the introduced cathode computational screening approach. The screening approach also identified promising Mg-ion transport in a family of materials, ABO_4 zircons, which had not previously been considered as Mg intercalation cathodes. Studying the diffusion properties of these materials yielded valuable insights into a new structural design metric to improve Mg-ion transport. The final chapter summarizes significant conclusions in this body of work and outlines potential avenues for additional progress in cathode computational screenings.

2. High-throughput Screening Approach for Mg Cathodes[2]

2.1. Difficulties evaluating ionic mobility in cathode computational screenings

Computational methods that use density functional theory (DFT) to evaluate cathode properties of interest such as phase stability, voltage, capacity, and ionic diffusivity have been well established [36–38]. In the past 10-15 years, researchers began combining these methods in high-throughput computational screenings to evaluate various materials as cathodes which are enumerated in Table 2. For example in 2011, 277 mixed polyanionic compounds of the sidorenkite structure type were computationally screened as lithium and sodium cathodes where phase stability, voltage, and capacity properties were reported [39]. Follow-up work focused on carbonophosphates $Li_3MPO_4CO_3$ (M = transition metal) as a novel family of Li-ion cathode materials which also included the investigation of lithium mobility in one compound, $Li_xMn(PO_4)(CO_3)$, at various lithium concentrations (x = 1, 2, 3) [40]. There has also been interest in computationally screening sulfide and oxide spinels as multivalent cathodes where properties such as phase stability, voltage, and capacity were evaluated for a total of 56 compositions [18,31]. These properties were used to down select a smaller subset of 7 spinel hosts for investigating cation mobility. The computational exploration of six perovskites as Ca cathodes resulted in evaluating the Ca mobility in one composition identified as the most promising perovskite compound [41]. A high-throughput computational screening methodology for layered materials has also been reported for sodium and multivalent cathodes which included the calculation of migration barriers for 42 down selected layered materials [42,43]. A recent screening of polyanionic materials as K-ion cathodes used computational methods to down select candidate materials based on composition, stability, capacity, and voltage, at which point, 4 compounds were selected for experimental investigation [44]. Potassium mobility was computationally investigated for one compound.

Cathode Computational Screening	Publication Year	Total Materials Considered	Materials Evaluated with NEB
Li, Na: Sidorenkite family [39,40]	2011-2012	277	1
Multivalent: Spinels [18,31]	2015-2016	56	22
Ca: Perovskites [41]	2016	6	1
Na, Multivalent: Layered structures [42,43]	2018-2019	288	42
K: Polyanionic materials [44]	2021	74	1

Table 2. A summary of previous cathode computational screenings. Two notable observations include that these studies are each limited to a single structural family and that NEB calculations to evaluate transport properties are reserved for a smaller subset of the most promising candidates from the screening.

Across these efforts there has been a fundamental limitation insomuch that only one structural family, where the diffusion pathway and intercalation sites are already known, is considered. Recent work includes consideration of a wider range of structure types for Li-ion cathodes [45] and Mg-ion cathodes [46], however these materials all contained the working ion of interest where the intercalation sites are known.

---

[2] This chapter is closely adapted from Reference [10].

Cathode computational screenings that consider ionic mobility have typically used Nudged Elastic Band (NEB) calculations in conjunction with DFT to estimate the migration barrier [18,31,42,43,45,47]. NEB calculations are notoriously challenging due to the domain expertise required to inform the calculation inputs, their high computational cost, and numerical sensitivity that requires careful inspection of the calculation outputs. These challenges are evidenced by the number of cathode computational screenings that reserve performing NEB calculations for the single, most promising candidate [40,41,45], exclude ionic mobility entirely [38,39], or opted to pursue experimental electrochemical testing before performing a NEB calculation [44].

Given the challenges with NEB calculations, there have been several studies dedicated to acceleration efforts. The most common strategy to lower computational cost is usually to reduce the number of image relaxations along the predicted pathway. For example, some algorithms start with a lower image resolution that is iteratively increased such as in ANEBA [48] and AutoNEB [49]. In R-NEB, redundant image relaxations are avoided by using the system's reflection symmetry [50]. Machine learning has also been applied to approximate potential energy surfaces to more efficiently find the minimum energy pathway [51–53]. Compared to these approaches which rely on iterative interconnected image relaxations, ApproxNEB [54] is unique in that it evaluates images as single point calculations after an improved path initialization based on the material charge density.

An automated computational infrastructure for discovering intercalation electrodes has been previously reported [46], however these efforts have focused exclusively on evaluating materials in the discharged state where the intercalation sites are already known. Given the solid-state mobility challenges with multivalent ions, new strategies are needed to discover high-performance multivalent cathodes. In this chapter we report a new comprehensive computational framework for identifying novel multivalent cathode materials in compounds that do not a priori contain the working ion, e.g., are most stable in their charged state. This framework uses for the first time a combined methodology of the insertion algorithm [55] and the ApproxNEB algorithm [54] to screen by solid-state mobility properties in an automated high-throughput manner. We demonstrate our approach to computationally screen thousands of materials from the Materials Project database [56,57] in order to evaluate promising Mg cathodes.

2.2. A novel screening methodology to evaluate ionic mobility in high-throughput

The presented computational approach for evaluating materials free of magnesium as Mg cathodes can be described in four screening tiers. The criteria for each tier were ordered by a combination of robustness and computational cost. Less computationally demanding methods, which still correlate well to experimental results, were used first in earlier tiers in order to limit applying more expensive methods to a smaller number of candidate materials. Each tier focused on a different set of material properties, which are depicted in Figure 1, which will be described in more detail:

1. Relative stability and composition
2. Reducible specie oxidation state
3. Insertion site finding
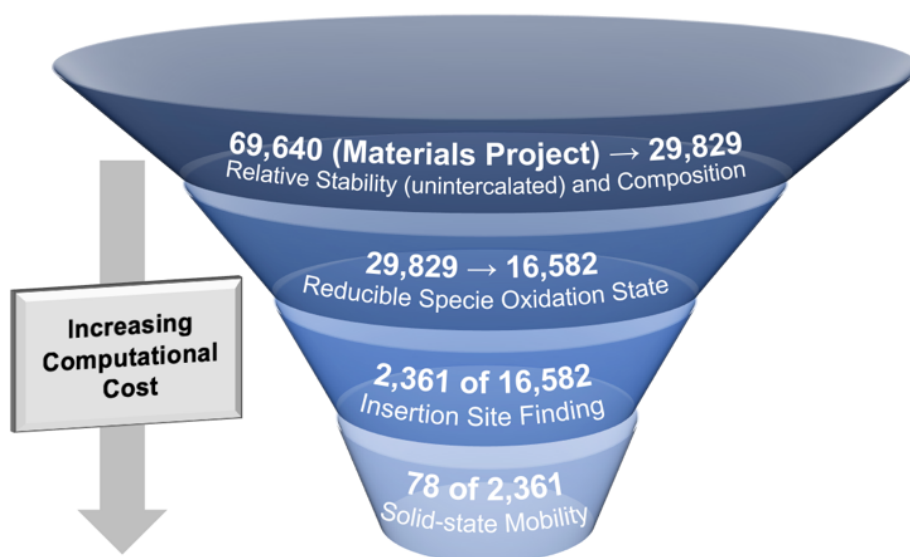4. Multivalent ion solid-state mobility

Figure 1. A funnel graphic summarizing the screening process for finding promising multivalent cathodes among materials in the deintercalated state. The screening process has been divided into four stages in order of increasing computational cost. The number of materials considered in each tier have been included for the described work on Mg cathodes to clarify the screening process and its limitations. However, we note that the exact numbers will change if the methodology is applied today as the number of materials in the Materials Project has almost doubled.

Relative Stability and Composition. The Materials Project, a database of DFT calculations of inorganic crystals and molecules, was used to source candidate materials [56,57]. Examination of Mg-free ("empty") hosts presents a vast space of many tens of thousands of possible materials compared to a much smaller number when limited to materials that already contain magnesium. Two properties, relative stability and composition, were used to narrow down this search space. Relative stability compared to other materials composed of the same elements was captured by the quantity, energy per atom above the convex hull, which encloses the most stable phases within the relevant chemical space [58,59]. This "energy above hull" is 0 eV/atom for a material that is predicted to be thermodynamically stable at 0 K. A cut-off value of < 0.2 eV/atom was used to select compounds that are likely to be synthesizable based on previous work that established sensible cut-off values [60,61]. Composition constraints were also applied that required the candidate material: 1) to contain at least one redox active element (Ti,

V, Cr, Mn, Fe, Co, Ni, Cu, Nb, Mo, Ru, Ag, W, Re, Sb, Bi), 2) to contain either oxygen or sulfur, and 3) excludes radioactive elements (elements with an atomic number between 84 and 104). Using these criteria, the Materials Project database (version 2018.11), which contained 69,640 inorganic crystals at the time that this work was started, was reduced to 29,829 candidate materials of interest.

Reducible Specie Oxidation State. Given the intention to insert magnesium into empty candidate host materials, viable candidates need to encompass a reducible specie that can accept electrons upon Mg insertion. The next screening tier is focused on finding materials with a high enough oxidation state to permit reduction. There are two algorithms within pymatgen [62] that are able to suggest likely oxidation states of a given material. One uses a bond valence method [63] to determine oxidation states and the other predicts appropriate oxidation states based on the material's chemical formula using a data mining approach. Candidate materials were discarded at this tier if they did not contain any of the following reducible species: Ti^{4+}, $V^{4+,5+}$, $Cr^{4+,5+,6+}$, $Mn^{3+,4+,5+,6+,7+}$, $Fe^{3+,4+,5+,6+}$, $Co^{3+,4+,5+}$, $Ni^{3+,4+}$, $Cu^{2+,3+,4+}$, Nb^{5+}, $Mo^{4+,5+,6+}$, $Ru^{5+,6+,7+,8+}$, $Ag^{2+,3+}$, W^{6+}, Re^{7+}, Sb^{5+}, $Bi^{4+,5+}$. Both methods were applied to evaluate oxidation states and in the case of disagreeing results, the bond valence method was preferred. Screening by reducible specie oxidation state narrowed the candidates of interest from 29,829 to 16,582 materials.

Insertion Site Finding. The next tier of screening candidate materials considers the identification of working ion insertion sites. Recently, Shen et al. reported a new approach for identifying the location of insertion sites in any given crystal structure which will be referred to as the "insertion algorithm" [55]. The insertion algorithm uses the calculated charge density of the material to identify charge density minima which were shown to correlate strongly with viable insertion sites in known electrode materials. For each possible insertion site, the working ion of interest (such as Mg in this case) is inserted with one working ion per unit cell. A DFT relaxation is then performed to refine the site location and evaluate the change in lattice and crystal structure to assess the possibility of viable insertion (whether the host structure is retained after insertion). As this tier requires multiple DFT calculations per material, it was not viable to apply the insertion algorithm to all 16,582 candidate materials at the time this preliminary work was performed. To demonstrate the screening workflow, the insertion algorithm was initially applied to a random selection of 2,361 materials. Given the investigation of empty cathodes that are more stable in their charged state, the insertion algorithm was set to explore the possibility of a single working ion per unit cell, as a first, necessary requirement. Further successive working ion insertions can be repeated until there is significant host structural change or the minimum redox state of the compound is reached, thus determining the maximum intercalation level.

Of the 2,361 materials where the insertion algorithm was applied, 1,767 were discarded because the host structure changed significantly upon insertion. Additional properties useful for screening become computable after completing the insertion algorithm for a material. These properties include the voltage and relative stability (energy above hull) of the partially/fully magnesiated compound. The remaining 594 candidate materials were prioritized for the last tier of evaluating Mg^{2+} solid-state mobility using the following criteria: 1) average voltage > 1.5 V, 2) energy per atom above the convex hull of the charged (unmagnesiated) material < 0.05 eV/atom, and 3) energy per atom above the convex hull of the discharged (magnesiated) material

< 0.1 eV/atom. After applying these criteria, the number of candidates was further reduced by using the structure matching capabilities in pymatgen [62] to select one material that would be representative of each unique structure type. As a result, 78 materials were selected for the next tier.

Applying the insertion algorithm to a host material produces a list of valid insertion sites for the working ion. These sites can be used to form a migration graph representing an interconnected network of Mg sites in the material as introduced in previous work [64]. Sets of neighboring Mg sites can be extracted from this migration graph which correspond to a segment of a possible Mg^{2+} migration pathway in the material. Images representing the Mg^{2+} in various positions along these pathway segments can be generated and paired with DFT calculations in order to evaluate the energetics along the pathway segment. This information provides a key input for evaluating Mg^{2+} solid-state mobility in a given material.

Multivalent Ion Solid-State Mobility. The last screening tier estimates the minimum energy barrier required for Mg^{2+} to migrate through the material and corresponds to the most computationally expensive tier. An upper limit migration barrier of 650 meV would remove materials which exhibit sluggish intrinsic ionic mobility and provide a possibility for good rate capability that might allow for a C/2 cycling rate with nanosized particles [19]. Given the evaluation of Mg-free compounds, only mobility in the charged (deintercalated) state at the dilute lattice limit was considered. Supercells were generated using pymatgen [62] to avoid fictious self-interaction effects from a neighboring Mg^{2+} due to periodic boundary conditions. Finally, the ApproxNEB algorithm [54] implemented through the python package, Atomate [65], was used to evaluate the migration barrier for a given pathway segment.

The ApproxNEB algorithm was selected over the traditional NEB scheme due to its lower computational cost and robustness which makes it more appropriate for high-throughput applications [54]. Initial benchmarking work to compare the ApproxNEB algorithm to NEB for 3 known Mg and Ca cathode systems found that ApproxNEB required ~5% of the computational resources compared to NEB (determined by considering the product of the number of nodes and wall time for running all calculations) and predicted energetic barriers within 150 meV of the NEB calculated values. This benchmarking data is provided in the Appendix 7.1. Implemented in Atomate, the ApproxNEB algorithm performs a series of relaxations for host, end point, and image structures for the specified migration events in a material. Additional ApproxNEB calculation details are included in Appendix 7.3. The key difference between NEB and ApproxNEB is in how the image relaxations are handled. With ApproxNEB, the images are relaxed independently of each other, and a coherent mobile ion path is maintained by fixing the positions of 2 atoms (the mobile working ion and the atom furthest away) in each image relaxation. Given the constraints of the ApproxNEB image relaxations, this method is likely to provide a slight overestimation of the energy barrier as compared to NEB. The energies produced by the ApproxNEB algorithm were mapped back onto the connections in the migration graph for a material. Pathway segments with incomplete points where calculations failed to reach sufficient convergence were excluded. The migration graph populated with the available energy information was used to locate the migration pathway through a material with the lowest barrier.

2.3. Material candidates to illustrate and validate screening approach

From the initial data set generated by the described screening process, 14 candidate materials were found to exhibit viable pathways for Mg^{2+} migration (ApproxNEB estimated barriers < 800meV). A few of these materials were identified as novel and pursued electrochemically. Further investigations into two of these novel materials, ε-VOPO$_4$ (mp-556459) and zircon EuCrO$_4$ (mp-22586), are described later in Chapters 3 and 4. In the remainder of this chapter, four materials as discussed in detail as a representative set to showcase the diversity of crystal structures, energy content, site topology and percolation pathways that can be assessed with this novel screening methodology. These four materials: V$_2$(PO$_4$)$_3$ (mp-26962), NaMn$_4$O$_8$ (mp-1016155), MnPO$_4$F (mp-25426), and MnO$_2$ (mp-25275) which are depicted in Figure 2, are highlighted here as candidate Mg cathodes to illustrate the value of this screening approach. Table 3 summarizes the following properties of these cathodes: voltage, capacity (upon a single Mg insertion), charge (deintercalated) stability, discharge (intercalated) stability, and the estimated ApproxNEB energetic barrier for Mg^{2+} migration. Figure 3 shows the migration energy landscape determined with the ApproxNEB algorithm for Mg^{2+} along the best percolating path identified.

Material	Voltage	Capacity	Charge (Deintercalated) Stability	Discharge (Intercalated) Stability	Energetic Barrier (dilute lattice limit)
Monoclinic NASICON Mg$_{(x<0.5)}$V$_2$(PO$_4$)$_3$ mp-26962	3.3 V	67 mAh/g	23 meV/atom	0 meV/atom	671 meV
Sodiated Birnessite Mg$_{(x<1)}$NaMn$_4$O$_8$ mp-1016155	2.2 V	136 mAh/g	19 meV/atom	82 meV/atom	200 meV
Tavorite Mg$_{(x<0.5)}$MnPO$_4$F mp-25426	3.7 V	148 mAh/g	42 meV/atom	62 meV/atom	1015 meV
Spinel Mg$_{(x<0.5)}$MnO$_2$ mp-25275	2.9 V	144 mAh/g	51 meV/atom	45 meV/atom	711 meV

Table 3. A summary of electrode properties of the four Mg cathodes that will be described in more detail. The voltage reported is a theoretical voltage (V) calculated from the energy difference of the intercalation reaction ($\Delta G_{rxn} = -nFV$). The theoretical capacity (Q) was calculated based on the atomic mass of the intercalated material (M) with $Q = nF/M$ based on the composition listed in the first column of Table 3. F is Faraday's constant and n represents the number of electrons transferred (for Mg, n=2). Stability values (energy per atom above the convex hull) were calculated using the MP2020Compatibility scheme [66] and Materials Project database phase diagrams using pymatgen [62] The lowest energetic barrier for Mg^{2+} migrating along a percolating pathway calculated with ApproxNEB at the dilute lattice limit (single Mg in host material supercell) is listed.
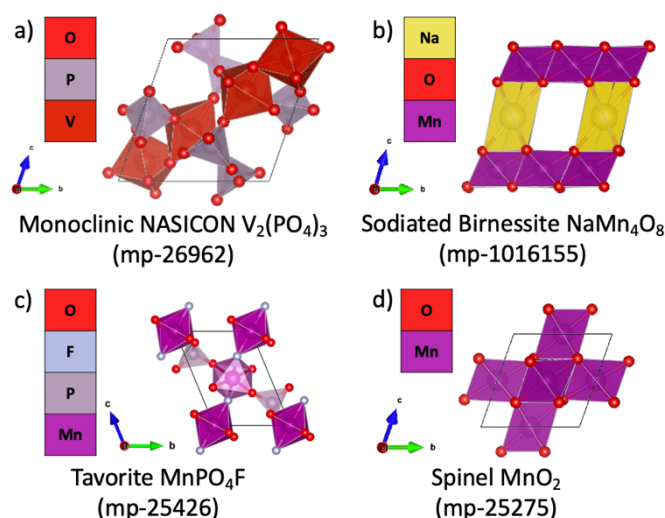
Figure 2. Unit cell crystal structures of each highlighted material in their unintercalated form are shown, including identifiers from the Materials Project: a) monoclinic NASICON $V_2(PO_4)_3$ from mp-26962, b) sodiated birnessite $NaMn_4O_8$ from mp-1016155, c) tavorite $MnPO_4F$ from mp-25426, d) spinel MnO_2 from mp-25275.
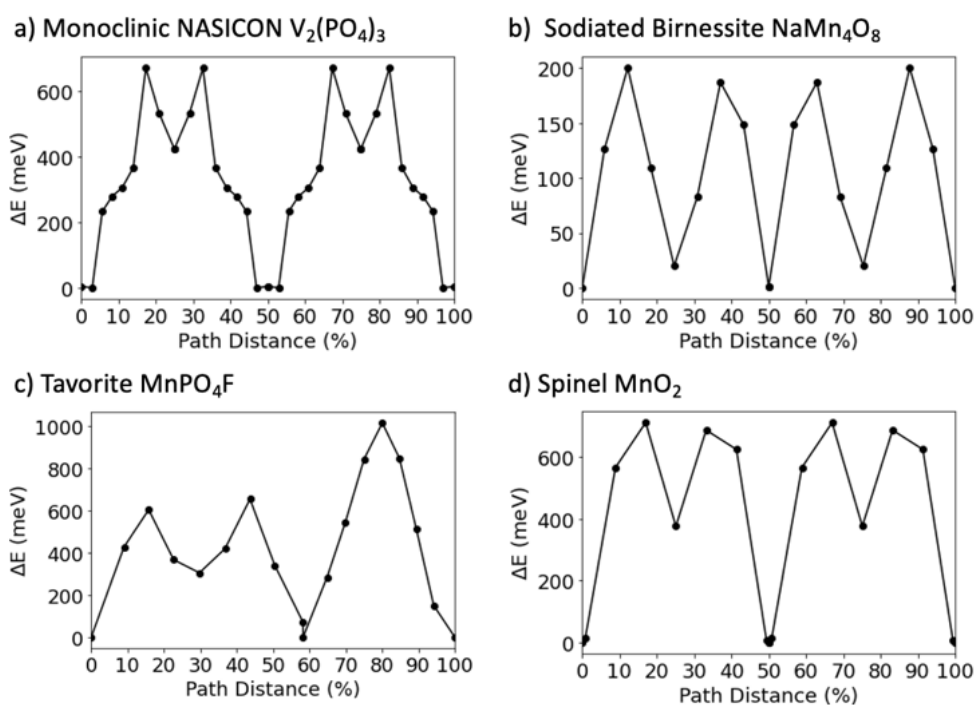

Figure 3. Plots of the energy landscape of Mg^{2+} migration along a percolating path for the 4 candidate materials. The percolating path starts from a given Mg site in a unit cell to the equivalent site in a neighboring unit cell and the energy evolution along the path is predicted with ApproxNEB at the dilute lattice limit (single Mg in host material supercell). Pathways were reduced to symmetrically distinct hops which were calculated separately and then mapped back to the pathway for computational efficiency by avoiding redundant calculations. Lines connecting adjacent points are provided as a guide to the eye. a) Monoclinic NASICON $V_2(PO_4)_3$ (mp-26962) has an energetic barrier of 671 meV along a total path distance of 13.2 Å. b) Sodiated Birnessite $NaMn_4O_8$ (mp-1016155) has an energetic barrier of 200 meV along a total path distance of 6.8 Å. c) Tavorite $MnPO_4F$ (mp-25426) has an energetic barrier of 1015 meV along a total path distance of 7.8 Å. d) Spinel MnO_2 (mp-25275) has an energetic barrier of 711 meV along a total path distance of 7.4 Å.

V$_2$(PO4)$_3$ (mp-26962) is a monoclinic NASICON that can be obtained experimentally from its lithiated version, Li$_3$V$_2$(PO$_4$)$_3$. This material has been studied as a Mg cathode where XAS spectra showed a change in vanadium oxidation state upon Mg intercalation [67], however definitive evidence of reversible Mg intercalation with repeated cycling has yet to be reported [8]. The voltage predicted by the screening process (3.3 V) compares well with the experimentally measured value of ~3.0 V vs. Mg/Mg^{2+}. Due to the single Mg insertion explored here, the calculated capacity corresponds to a lower limit magnesiation level of Mg$_{(x<0.5)}$V$_2$(PO$_4$)$_3$ and hence is below the experimentally reported capacity of ~197 mAh/g for Mg$_{(x<1.5)}$V$_2$(PO$_4$)$_3$. Sufficient Mg^{2+} mobility for acceptable rate capability appears possible with an ApproxNEB predicted migration barrier of 671 meV. While this value is greater than the 650 meV threshold, as stated previously, ApproxNEB is known for overestimating the energy barrier; hence it is likely the true activation energy for dilute Mg^{2+} migration is lower. The results of this screening recommends further investigation of V$_2$(PO$_4$)$_3$ as a Mg cathode, particularly highlighting the need for testing in electrolytes that are stable at sufficiently high voltages.

NaMn$_4$O$_8$ (mp-1016155) is a sodiated version of birnessite, δ-MnO$_2$, which is the layered polymorph of MnO$_2$. Birnessite is typically hydrated with water molecules between layers of MnO$_6$ octahedra and has been studied in the literature as a Mg cathode [8,68,69]. More success has been found using aqueous electrolytes where there is a reversible transformation from δ-MnO$_2$ to λ-MnO$_2$ upon discharge [68]. The inclusion of crystalline water increases the interlayer spacing [70] which could be favorable for ion mobility, however involving water presents a challenge for using birnessite in high-energy-density Mg batteries given the incompatibility of water with magnesium metal anodes. However, pillaring the structure with sodium ions instead of water molecules avoids these compatibility issues and may help explain the good Mg^{2+} mobility predicted by a low ApproxNEB migration barrier of 200 meV. Alkali-ion pillaring has been examined as a strategy to improve electrochemical performance in vanadium oxides as Li-ion cathodes by stabilizing the structure and improving ion mobility [71–73]. More detailed studies would be required to understand the role of sodium and possible avenues for facilitating multivalent ion mobility such as in NASICONs where sodium reordering upon calcium transport has been demonstrated [74–76]. Replacing water with sodium in the birnessite structure could offer an avenue for using the layered δ-MnO$_2$ polymorph as a cathode with magnesium metal anodes. While the synthesis of various sodiated versions of birnessite have been reported [77], electrochemical investigation has been limited to consideration as a Na cathode [70,78,79].

MnPO$_4$F (mp-25426) belongs to the tavorite structure family. This class of materials has been studied as Li-ion cathodes and includes examples such as LiVPO$_4$F [80], LiFePO$_4$F [81], and LiFeSO$_4$F [82]. Theoretical work on FeSO$_4$F [83] and VPO$_4$F [84] as Mg cathodes has been reported and found promising properties. However, no Mg^{2+} electrochemical experimental work has yet been published on these materials [8]. With voltages of 2.5 V for FeSO$_4$F and 2.6 V for VPO$_4$F, perhaps difficulties in identifying higher voltage magnesium electrolytes present a roadblock. With a predicted voltage of 3.7 V for MnPO$_4$F, the lack of suitable electrolytes is also a limitation that must be overcome before this material can be pursued experimentally. While reasonable Mg^{2+} migration barriers have been identified for other tavorites (360 meV for FeSO$_4$F and 704 meV for VPO$_4$F), the dilute lattice limit ApproxNEB barrier of 1015 meV for MnPO$_4$F

is prohibitively high. Although MnPO$_4$F is an attractive cathode candidate from an energy density perspective, its poor solid-state Mg^{2+} mobility would result in poor rate capability.

MnO$_2$ (mp-25275) is the spinel polymorph or λ phase of MnO$_2$. Given that spinel LiMn$_2$O$_4$ is a well-studied, commercialized lithium-ion cathode [85], there has been significant interest in studying spinels as Mg cathodes [19,31,86]. While promising from an energy density standpoint with a voltage of 2.9 V vs. Mg/Mg^{2+} and theoretical capacity of 144 mAh/g, it has been challenging to experimentally realize a high capacity with repeated cycling because of sluggish Mg^{2+} solid-state mobility [8]. High Mg^{2+} migration barriers of ~800 meV for the dilute lattice limit (charged/deintercalated state) calculated with NEB have been reported for spinel MgMn$_2$O$_4$ [19,31] which is consistent with the high (> 650 meV) migration barrier of 711 meV predicted by ApproxNEB in this screening method. This λ-MnO$_2$ spinel example demonstrates the value of the fourth screening tier where ApproxNEB is used to estimate migration barriers to identify materials where Mg^{2+} solid-state mobility will be a challenge.

2.4. Preliminary insights into the role of site volume & low coordination points

The migration pathways and relaxed ApproxNEB image structures were examined in more detail for the 4 highlighted Mg cathode candidates: NASICON V$_2$(PO$_4$)$_3$ (mp-26962), birnessite NaMn$_4$O$_8$ (mp-1016155), tavorite MnPO$_4$F (mp-25426), and spinel MnO$_2$ (mp-25275). In addition to mapping the energy difference along the pathway, the volume associated with the mobile Mg^{2+} calculated using the Voronoi algorithm through pymatgen is included [62,87–89]. The graph area is colored to reflect the coordination of the Mg^{2+} at various positions along the path based on the relaxed ApproxNEB images, where the coordination number was analyzed using the CrystalNN algorithm in pymatgen [62,87]. Images of the mobile Mg^{2+} in the host crystal structure made using the VESTA software at significant points along the migration path are marked by letters and displayed with these plots in Figure 4.
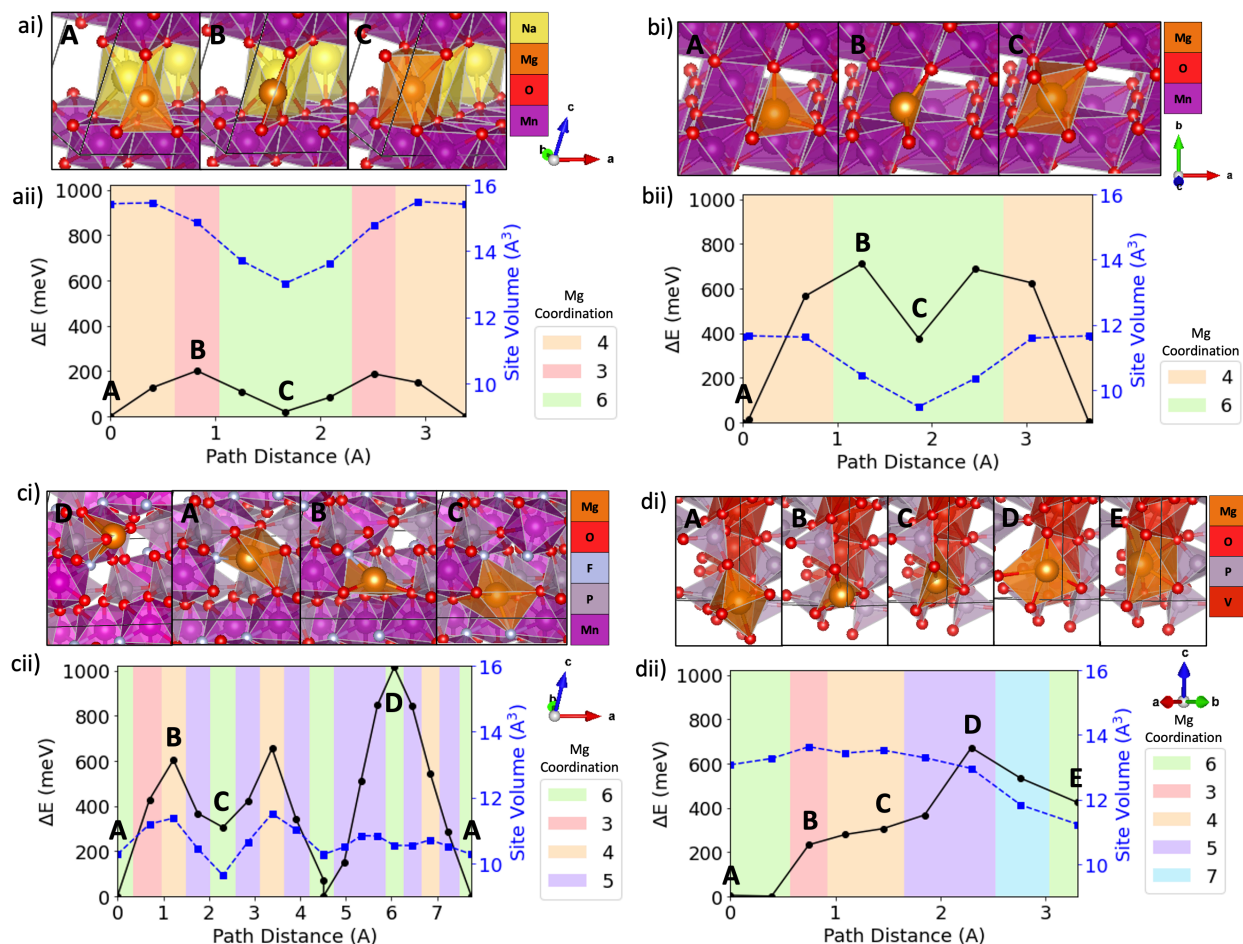
Figure 4. The evolving environment and associated Mg^{2+} migration energy as a function of pathway coordinate in a) sodiated birnessite $NaMn_4O_8$, b) spinel MnO_2, c) tavorite $MnPO_4F$, and d) NASICON $V_2(PO4)_3$. For each material, i) depicts a graph of the energy barrier (solid black line with circles), Mg site volume (dashed blue line with squares), and Mg^{2+} coordination (colored graph area) based on ApproxNEB and ii) shows images of the Mg^{2+} at various positions along the migration pathway (labeled by letters).

A common feature in the pathways examined is the occurrence of high-energy (bottleneck) ion positions where the energy difference is highest (e.g. Figure 4a position B for sodiated birnessite $NaMn_4O_8$, Figure 4b position B for spinel MnO_2, Figure 4c position B & D for tavorite $MnPO_4F$, Figure 4d position B & D for NASICON $V_2(PO4)_3$) as the mobile Mg^{2+} passes through a plane of anions. In the case where the Mg^{2+} is moving from a tetrahedral to an octahedral site where the tetrahedra and octahedra are face sharing, this highest-energy point corresponds to the Mg^{2+} squeezing through the triangle of anions composing the shared face. This finding is in line with previous work on spinels where the area of the anion triangle was expanded by substituting larger and more polarizable anion atoms in order to lower the energetic penalty for migration [90]. One counterintuitive finding, however, is that these bottleneck migration ion events do not correspond with the lowest volume sites along the migration path. In the identified pathways of these four materials, these lowest volume sites occur when Mg^{2+} is in a 6-fold site of favored coordination, indicating a site with particularly favorable Mg-anion coordination and correspondingly tight bond lengths. This suggests that volume alone may not be a meaningful descriptor and more significant conclusions can be made by comparing volume across sites with similar local bonding environments.

The identified pathways for sodiated birnessite $NaMn_4O_8$ and spinel MnO_2 are both composed of face-sharing tetrahedra (tet) and octahedra (oct). While these two materials exhibit similar tet-oct-tet coordination changes, sodiated birnessite $NaMn_4O_8$ exhibits a much lower Mg^{2+} ApproxNEB migration barrier (200meV) compared to spinel MnO_2 (711meV). One possible explanation is that the sodium in birnessite expands the interlayer spacing, reduces the electrostatic interaction between Mg^{2+} and the oxygen layers, and increases the available volume along the pathway compared to spinel MnO_2. Therefore, the energy penalty for Mg^{2+} migration is lowered because the Coulombic interactions between the mobile ion and host structure are weaker.

Examining the high energy positions in tavorite $MnPO_4F$ illustrates the influence of anion composition when considering Mg^{2+} passing through planes of anions. In Figure 4c, the higher-energy bottleneck position D corresponds to the mobile Mg^{2+} passing through a plane of 4 oxygen atoms. The Mg^{2+} moves through a plane comprising of 2 oxygens and one fluorine at the lower energy bottleneck position B. At D, the Mg^{2+} ion passes through the oxygen plane off center while at position B, the Mg^{2+} ion is in the center of the anion triangle. Therefore, it is likely this position discrepancy contributes to the higher energy of point D, but it is also possible that substituting fluorine for one oxygen in the anion plane reduces the energetic penalty.

Of the 6 identified bottleneck positions where the mobile Mg^{2+} ion passes through an anion plane and experiences a lower coordination in these 4 materials, only one case, point B of Figure 4d for NASICON $V_2(PO4)_3$, does not correspond to a local energy maximum. We hypothesize that the relatively larger available volume for the mobile Mg^{2+} in NASICON $V_2(PO4)_3$ is responsible for the improved migration energetics, even when moving through anion planes. Both NASICON $V_2(PO4)_3$ and sodiated birnessite $NaMn_4O_8$ exhibit large volume Mg sites (> 13 A^3) as compared to spinel MnO_2 and tavorite $MnPO_4F$ (< 12 A^3). The Mg sites exhibit larger volumes (> 13 A^3) and relatively low energy differences (< 350 meV) when considering the NASICON $V_2(PO4)_3$ oct-tet transition (Figure 4d A$\rightarrow$B$\rightarrow$C) and the sodiated birnessite $NaMn_4O_8$ tet-oct transition (Figure 4a A$\rightarrow$B$\rightarrow$C). Thus, the tetrahedra and octahedra volumes are large enough to avoid a substantial energy penalty when the Mg^{2+} squeezes through the shared anion face. This suggests that perhaps there is a minimum anion triangle area where a costly energy penalty for Mg^{2+} migration can be avoided.

From the reported work on Mg cathodes, four materials: NASICON $V_2(PO4)_3$ (mp-26962), birnessite $NaMn_4O_8$ (mp-1016155), tavorite $MnPO_4F$ (mp-25426), and spinel MnO_2 (mp-25275) were identified as possible Mg cathodes and discussed in more detail. Experimental reports on NASICON $V_2(PO4)_3$ and spinel MnO_2 validate the evaluation of these materials with the developed computational screening framework. NASICON $V_2(PO4)_3$ and birnessite $NaMn_4O_8$ were identified as promising Mg cathodes that warrant further experimental investigation. Among these examples, different Mg^{2+} migration barriers were observed in birnessite $NaMn_4O_8$ and spinel MnO_2 despite having similar changes in coordination along the pathway. Local energy maxima were found to correlate with site topology (such as passing through an anion plane or point of lower coordination) rather than the lowest site volume along the path. However, when comparing only the anion plane sites, materials which exhibit a larger area between anions (such as NASICON $V_2(PO4)_3$ and birnessite $NaMn_4O_8$) were found to

reduce the energy penalty for Mg^{2+} migration. Therefore, the available free volume for a given type of local bonding environment of a mobile ion site in the host structure was proposed as another influential factor for improving solid-state mobility.

2.5. Mg cathode data set with phase stability, energy density, & transport properties

In establishing this computational screening methodology, only an initial subset of candidate Mg cathode materials were considered. Given available resources at the time, the insertion workflow was only applied to 2,361 host materials and ultimately 78 unique structures were evaluated with the ApproxNEB workflow. After this preliminary work, additional materials were evaluated with this screening approach resulting in a larger Mg cathode data set. 5,853 empty host materials of the 16,682 materials previously down selected based on their reducible species oxidation state were prioritized for Mg insertions based on excluding candidates which contained an extractable ion (H, Li, Na, K, Rb, Cs, Mg, Ca, Cs, Ag, Cu). Of these 5,863 attempted Mg insertion workflows, 83% resulted in at least one viable Mg site. This ultimately resulted in 4,872 Mg cathodes from which 229 ApproxNEB workflows were attempted. There were 193 unique structure types in these 229 candidates. All ApproxNEB images calculations successfully completed for 97 electrodes, which contained 85 unique structure types. This dataset of Mg cathodes with phase stability, energy density, and transport properties is available through MPContribs on the Materials Project [56,57] under the title "Mg Cathode Screening 2022."

3. An illustrative example of further investigating ε-Mg$_x$VOPO$_4$[3]

3.1. Background and previous work on VOPO$_4$ polymorphs as cathodes

There are seven distinct polymorphs of VOPO$_4$: α$_I$ (P4/n), α$_{II}$ (P4/n), β (Pnma), δ (P42/mbc), ε (Cc), ω (P42/mmc) and ɣ (Pbam). The α$_I$, β, ε, polymorphs are the most thoroughly studied because they are the only stable polymorphs [91,92]. VOPO$_4$ polymorphs have been previously studied in the literature with an emphasis on their electrochemical properties as lithium and sodium cathodes [91–93]. Standard properties calculated by DFT are available for these VOPO$_4$ polymorphs in the Materials Project [56,57] using the following identifiers: mp-559299 for α$_I$, mp-25265 for β, and mp-556459 for ε. The α$_I$ polymorph is a layered structure composed of VO$_5$–PO$_4$ units. The β and ε polymorphs are structurally similar as both are compared of 3D network of VO$_6$–PO$_4$ units. β-VOPO$_4$ is more stable than ε-VOPO$_4$, however both polymorphs can be experimentally accessed based on the synthesis conditions [92]. The ε-VOPO$_4$ structure also has two possible monoclinic space groups. The Cc space group considered here is more stable than the P2$_1$/n space group according to DFT calculations [92]. While the α$_I$ polymorph has been previously studied as a Mg cathode [94,95], to our knowledge, ε-VOPO$_4$ has not previously been considered as a Mg intercalation cathode.

3.2. Additional insertion and NEB calculations to computationally investigate ε-Mg$_x$VOPO$_4$

ε-VOPO$_4$ (mp-556459) was identified as a promising Mg cathode candidate through the previously introduced novel computational screening methodology for multivalent cathodes [10]. The following properties were calculated with DFT calculations through this screening methodology with additional details provided in Appendix 7.2. Phase stability of ε-VOPO$_4$ was 3 meV/atom and 25 meV/atom for ε-Mg$_{0.5}$VOPO$_4$ based on the energy per atom above the convex hull calculated using phase diagrams from the Materials Project [56,57] and the MP2020 Compatibility scheme [66]. A voltage of 2.7 V and capacity of 166 mAh/g was predicted for ε-VOPO$_4 \Leftrightarrow$ ε-Mg$_{0.5}$VOPO$_4$. The Mg^{2+} migration barrier at the dilute lattice limit was estimated to be 883 meV using ApproxNEB [54] and the corresponding energy profile is shown in Figure 5. The pathway identified by ApproxNEB is composed of ~4.3 Å hops between equivalent sites in a 1-dimensional channel that is in the same cavity as a pathway previously reported for lithium composed of "Li1" sites [96]. The investigated diffusion pathway in ε-Mg$_x$VOPO$_4$ is depicted in Figure 6.

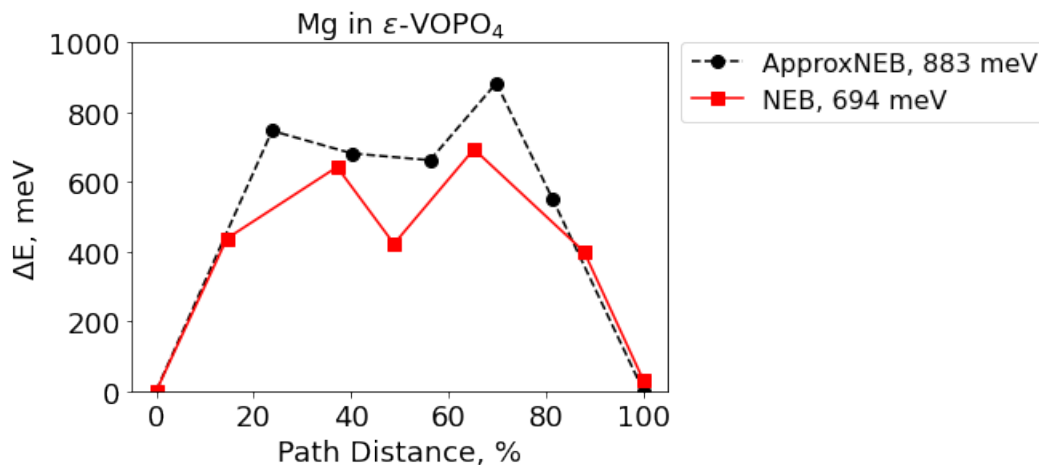[3] Portions of this chapter are adapted from Reference [97].

Figure 5. A comparison of the energy profile and Mg^{2+} migration barriers predicted by the Mg cathode screening approach with the ApproxNEB workflow (black circles, dashed lines) and traditional DFT-NEB (red squares, solid lines) for ε-Mg_xVOPO4 at the dilute lattice limit (single Mg-ion in supercell). The total path distance is ~4.3 Å.
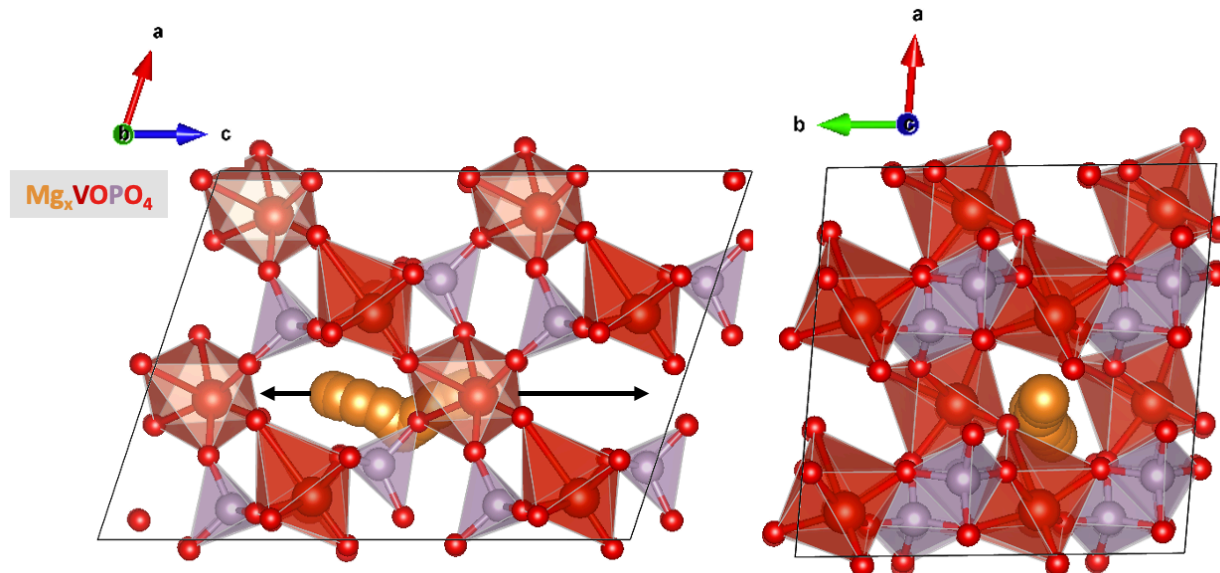

Figure 6. Supercell structures of ε-Mg_xVOPO4 illustrating the pathway investigated which is a 1-dimensional channel oriented along the c-axis. Mg atoms (in orange) are placed to show the connection between equivalent sites which have a distance of ~4.3 Å.

After identifying ε-Mg_xVOPO_4 as a possible Mg cathode of interest, additional insertion algorithm workflow calculations [55], which are described in Appendix 7.2, were performed to determine the phase stability and voltage profile at higher magnesium concentrations. The phase stability of ε-$MgVOPO_4$ was 14 meV/atom indicating this intercalation level is still viable. However, higher Mg concentrations are unlikely given the phase stability of ε-$Mg_{1.5}VOPO_4$ was found to be prohibitively metastable at 164 meV/atom. Therefore, only calculations for ε-$Mg_{x\leq1}VOPO_4$ are included. DFT calculations predicted a voltage of 2.6 V for ε-$Mg_{0.5}VOPO_4 \Leftrightarrow$ ε-$MgVOPO_4$ which would correspond to an additional 166 mAh/g of capacity. Overall, an average voltage of 2.7 V and gravimetric capacity of 331 mAh/g was predicted for ε-$VOPO_4 \Leftrightarrow$ ε-$MgVOPO_4$. The full voltage profile predicted by DFT is shown in Figure 7.
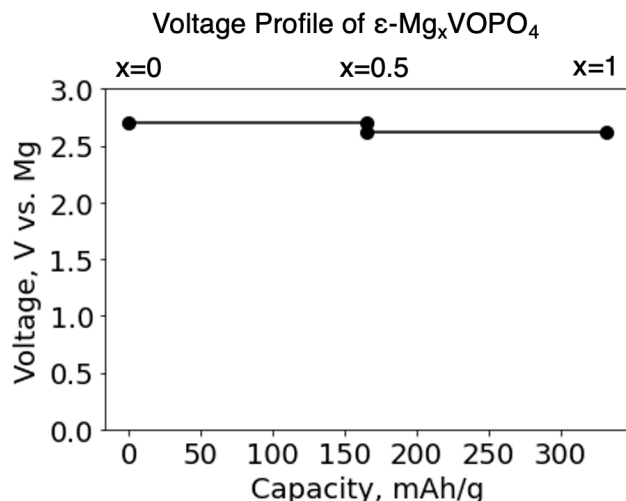
Voltage Profile of ε-Mg$_x$VOPO$_4$

Figure 7. Theoretical voltage profile based on DFT calculations for ε-Mg$_x$VOPO$_4$. Two phase regions are identified between ε-VOPO$_4$ ⟺ ε-Mg$_{0.5}$VOPO$_4$ and ε-Mg$_{0.5}$VOPO$_4$ ⟺ ε-MgVOPO$_4$ for an overall average voltage of 2.7 and gravimetric capacity of 331 mAh/g.

NEB calculations were performed (also at the dilute lattice limit) to better characterize the ion mobility properties. 2x2x2 supercells resulting in a total of 113 atoms (1 Mg per 16 VOPO$_4$ formula units) were used. After the first NEB calculation, the intermediate local energy minima image was relaxed as an end point to break-up the pathway into two segments for a more refined Climbing Image NEB (CI-NEB) calculation. Additional calculation details are outlined in Appendix 7.4. As expected, the Mg^{2+} migration barrier of 883 meV for the dilute lattice limited (single working ion in the supercell) predicted by ApproxNEB is an overestimate compared to more refined methods such as NEB which is shown in Figure 5. The NEB calculation found the Mg^{2+} migration barrier to be 694 meV which was further refined to 687 meV with CI-NEB. Given ε-VOPO$_4$ has been previously investigated as cathode with lithium and sodium, CI-NEB calculations with Li and Na are also included for comparison with Mg in Figure 8. Using the method for estimating diffusivity by Rong et al. [54], a barrier of 687 meV would result in D ~ 3 x 10^{-15} cms^2/s. This diffusivity would be sufficient for at least a C/8 cycling rate at room temperature with 100 nm sized particles.
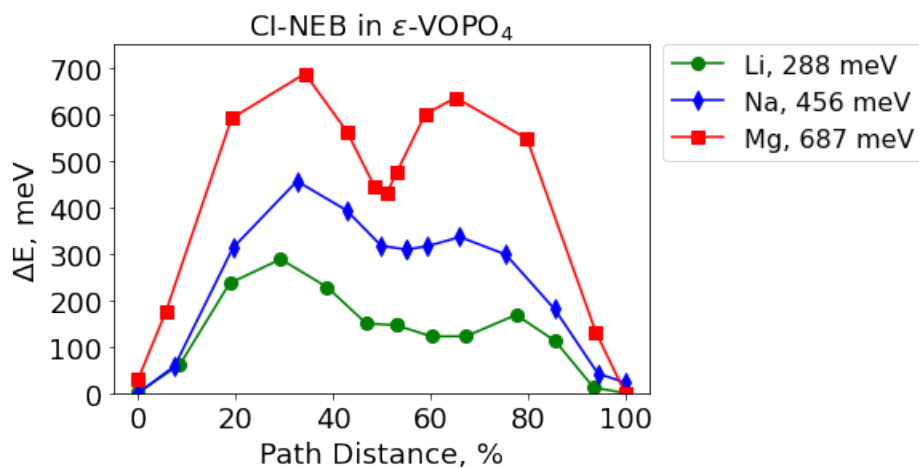
CI-NEB in ε-VOPO$_4$

Figure 8. CI-NEB results for ε-VOPO4 at the dilute lattice limit (single working ion in supercell) for Li (green circles), Na (blue diamonds), and Mg (red squares). The total path distance is ~4.3 Å.

3.3. Attractive energy density properties in ε-Mg$_x$VOPO$_4$

The energy density properties of ε-Mg$_x$VOPO$_4$ are attractive with a theoretically predicted voltage of 2.7 V vs. Mg/Mg^{2+} and 331 mAh/g. The higher voltage is a notable improvement over the sulfide magnesium cathodes discussed in the introduction, although perhaps not surprising given that ε-Mg$_x$VOPO$_4$ is an oxide. Although with a Mg^{2+} migration barrier of 687 meV, the intrinsic transport properties of ε-Mg$_x$VOPO$_4$ are not as promising as the original Chevrel Mg$_x$Mo$_6$S$_8$ cathode, which demonstrated stable and reversible room temperature cycling [7,15]. Initial experimental investigations into hydrothermally synthesized ε-VOPO$_4$ verified reversible Mg intercalation and found the best electrochemical performance after initial pre-cycling with Na [97]. An initial capacity of 90 mAh/g and average voltage of -0.1 V vs. activated carbon (~2.3V vs Mg^{2+}/Mg) was experimentally measured [97]. While these energy density properties are a significant advancement over Chevrel Mg$_x$Mo$_6$S$_8$, they can be further improved to optimize the performance of ε-Mg$_x$VOPO$_4$. For example, processing improvements to achieve uniform particle sizes below 100 nms may be critical to improving cell rate capability given the higher migration barrier of 687 meV for ε-Mg$_x$VOPO$_4$. While there are limitations in this initial experimental investigation, the identification of ε-Mg$_x$VOPO$_4$ as a higher voltage Mg cathode is an exciting finding that illustrates the value of the introduced novel computational cathode screening approach.

4. Strategies to Improve Transport Informed by ABO_4 Zircons[4]

4.1. Established material design rules for better multivalent ion mobility

Given the transport challenges inherent to more polarizing multivalent ions (compared to Li^+), recent efforts have been dedicated to understanding and improving the solid-state mobility of multivalent ions, especially in oxide hosts. Common material design strategies [5] include: 1) using materials with larger anions, which allow for better screening, in the host framework (e.g., opting for sulfides or selenides over oxides) and 2) leveraging the coordination preference of a specific cation to improve transport. For example, Mg^{2+} has a strong preference for octahedral local bonding environments [98,99], which usually results in poor mobility and difficult extraction of Mg^{2+} from octahedral sites.

High energy sites along the diffusion pathway in a material can also correspond to the mobile cation passing through points of lower coordination. These lower coordination points may represent a position where the mobile cation passes through a plane of neighboring anions [10]. For example, in the structural motif where a diffusion pathway is composed of edge-sharing octahedra as illustrated in Figure 9a, the lowest coordination occurs when the mobile cation passes through a triangular plane of 3 anions. This triangular plane is the shared face between the octahedral and intermediate tetrahedral site and corresponds to the highest energy point along the migration pathway in several materials with this edge-sharing octahedral motif [19]. Materials with larger anions of the same charge are better at screening unfavorable electrostatic interactions at these bottlenecks which usually results in improved transport properties. While understanding of the connection between various materials properties and multivalent ion transport is evolving, identifying materials with better transport properties based on these principles remains a challenge.
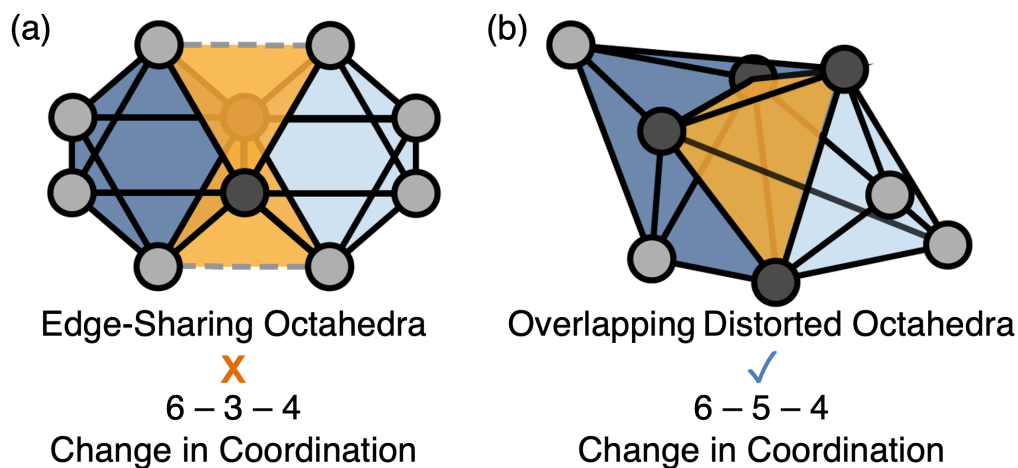
Figure 9. A visual representation of the characteristic structural motifs along diffusion pathways where the grey circles represent anions. Neighboring octahedral sites are colored different shades of blue while the intermediate tetrahedral sites are colored yellow. The darker grey colored circles indicate which anions are shared by both octahedra. (a) shows the edge-sharing octahedral motif found in previously studied cathodes (e.g., spinels, layered structures, olivines) where there is no shared volume with the intermediate tetrahedral site. (b) shows the overlapping distorted octahedral motif characteristic of zircons where volume is shared with the intermediate tetrahedral site.

---

[4] This chapter is closely adapted from Reference [114].

4.2. Screening approach identifies promising transport properties in ABO₄ Zircons

Our work introducing a computational screening approach to identify high-performance multivalent intercalation cathodes [10] has proved instrumental in evaluating solid-state mobility in a wider variety of structure types. A new family of materials with the ABO_4 zircon-type structure (with tetragonal space group I41/amd) was identified using this methodology, specifically for their predicted high Mg^{2+} mobility. Our subsequent investigation of these materials as Mg cathodes are reported in this chapter. The ABO_4 zircon structure is composed of edge-sharing alternating AO_8 dodecahedrons and BO_4 tetrahedrons which is illustrated in Figure 10, a depiction of the unit cell structure of zircon YVO_4. In the AO_8 dodecahedron, the A atom is 8-coordinated, while in the BO_4 tetrahedron, the B atom is 4-coordinated. These structures also exhibit interstitial sites of distorted octahedra and tetrahedrons which form one-dimensional channels [100], which are represented in Figure 9b.
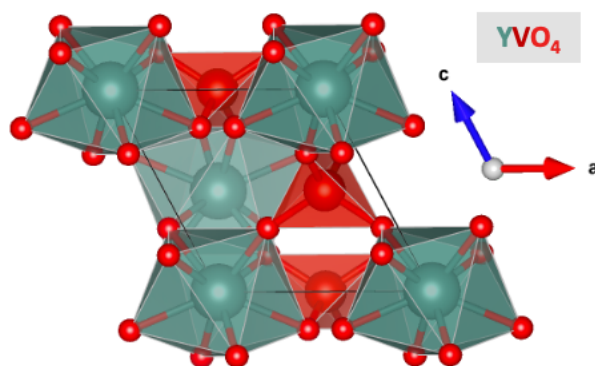

Figure 10. A unit cell structure of YVO_4 showing the ABO_4 zircon-type structure (with tetragonal space group I41/amd) composed of edge-sharing alternating AO_8 dodecahedrons and BO_4 tetrahedrons.

As illustrated in Figure 9, zircons present a unique structural motif compared to many previously studied cathodes (e.g., spinels, layered structures, olivines) with edge-sharing octahedral sites [19]. A key difference is that the tetrahedral and distorted octahedral interstitial sites of the zircon structure are overlapping in volume, in contrast to the absence of shared volume in materials with edge-sharing octahedral interstitial sites, which are connected by face-sharing tetrahedral sites. The prototype zircon is $ZrSiO_4$, a naturally occurring mineral [101], spanning a wide range of chemistries. This work focuses on a smaller subset of zircons (A = Y, Eu and B = V, Cr) which contain a redox-active cation and can be synthesized through previously reported methods [102].

The four zircon materials which are the focus of this work have been available in the Materials Project with standard properties calculated by DFT [56,57]. In addition, the structural, mechanical, electronic, magnetic, and optical properties of zircons have previously been investigated, including YVO_4 [103,104], $EuVO_4$, [105–107] $YCrO_4$, [101,108] and $EuCrO_4$ [109,110]. Comparatively, there is less work regarding the electrochemical and transport properties of zircons required to inform their performance as intercalation cathodes. Oxygen diffusivity has been measured for zircon EuVO4 [106] and the conductivity of interstitial H^+, Li^+, Na^+, Mg^{2+}, Ca^{2+}, was studied in zircon YPO_4 [111,112] (although YPO_4 lacks a redox active

species which is one of the requirements for a cathode). To our knowledge, this is the first reported work to consider zircon materials as intercalation cathodes for Mg.

4.3. Predicted phase stability upon Mg intercalation of ABO$_4$ zircons

The insertion algorithm [55] was used to evaluate the maximum viable concentration of Mg that could be introduced in YVO$_4$, EuVO$_4$, YCrO$_4$, and EuCrO$_4$. This workflow performs successive DFT calculations of Mg-ion insertions at candidate interstitial sites, which are identified by charge density minima in the host structure determined by DFT calculations. Further calculation details are provided in Appendix 7.2. A maximum of two Mg atoms (corresponding to a composition of MgABO$_4$) insertions were attempted to avoid exceeding the redox capabilities of the material where the B transition metal cannot be further reduced than $B^{5+} \rightarrow B^{3+}$. The insertions are deemed successful as long as the relaxed structure is similar (topotactic insertion) to the uninserted structure, the redox capability of the cations is not exceeded, and the energy above hull for the inserted material remains below a given cutoff value.

The "energy above hull," which is the energy per atom above the convex hull for a given material compared to the most stable phases in the relevant chemical space [58,59] provides a measure of phase stability. A lower energy above hull value corresponds to better phase stability as the minimum value of this quantity, 0 eV/atom, means a material is predicted to be the most thermodynamically stable phase at 0 K based on DFT calculations. Energy above hull values were calculated with the MP2020 compatibility scheme [66] and the Materials Project [56,57] database phase diagrams using pymatgen [62]. The energy above hull values for the Mg$_x$ABO$_4$ zircons of interest (A = Y, Eu and B = V, Cr) are reported for 3 magnesium concentrations (x = 0, 0.5, 1) in Table 4. In addition, if a material was not the most stable phase, the predicted decomposition products are included. Conversion voltages for the 4 zircons of interest were also calculated using pymatgen [62] and phase diagrams from the Materials Project [56,57]. The conversion voltages and their corresponding reactions are shown in Table 5.

ABO$_4$ Zircon	Phase Stability (meV/atom)			Decomposition Products
	ABO$_4$	Mg$_{0.5}$ABO$_4$	MgABO$_4$	
YVO$_4$ (mp-19133)	0	133	196	YVO$_3$ (mp-18883) MgO (mp-1265)
EuVO$_4$ (mp-22796)	0	0	-	-
YCrO$_4$ (mp-18825)	~0*	139	-	Y$_2$O$_3$ (mp-2652) YCrO$_4$ (mp-18825) MgCr$_2$O$_4$ (mp-19202) MgCrO$_4$ (mp-19120)
EuCrO$_4$ (mp-22586)	0.1	127	219	Eu$_2$O$_3$ (mp-1182469) EuCrO$_4$ (mp-22586) MgCr$_2$O$_4$ (mp-19202) MgO (mp-1265)

Table 4. Energy above hull values from DFT calculations combined with Materials Project [56,57] data to evaluate phase stability for Mg$_x$ABO$_4$ zircons (A = Y, Eu and B = V, Cr) at x = 0, 0.5, 1 magnesium concentrations. The decomposition products are included when a material was not the most stable phase at that composition. *Within our numerical accuracy YCrO$_4$ is degenerate with the hull.

Conversion Reaction	Conversion Voltage (V)
$2\ YVO_4 + 2\ Mg \rightarrow 2\ YVO_3 + 2\ MgO$	1.7
$2\ EuVO_4 + Mg \rightarrow Eu_2MgV_2O_8$	1.9
$2\ YCrO_4 + 1.25\ Mg \rightarrow Y_2O_3 + 0.5\ MgCrO_4 + 0.75\ MgCr_2O_4$	2.8
$2\ EuCrO_4 + 2\ Mg \rightarrow MgCr_2O_4 + Eu_2O_3 + MgO$	2.6

Table 5. Conversion reactions and voltages calculated from DFT for ABO_4 zircons (A = Y, Eu and B = V, Cr).

The insertion algorithm identified a single Mg-ion insertion per unit cell (2 ABO_4 formula units) in $EuVO_4$ and $YCrO_4$ resulting in a maximum intercalation level of $Mg_{0.5}ABO_4$. Two Mg-ion insertions could be tolerated in YVO_4 and $EuCrO_4$, for a maximum intercalation level of $MgABO_4$, and the phase stability evaluation indicates that a two-phase region of ABO_4 and $MgABO_4$ is more thermodynamically favorable which makes observing $Mg_{0.5}ABO_4$ unlikely. With the exception of $EuVO_4$, all energy above hull values upon magnesiation are >100 meV/atom which strongly indicates that further magnesiation is unfavorable and will result in phase decomposition [60,61]. The best phase stability was found in $EuVO_4$ where both $EuVO_4$ and $Mg_{0.5}EuVO_4$ were found to be the ground states with an energy above hull of 0 meV/atom. The conversion voltages of $YCrO_4$ (2.8 V) and $EuCrO_4$ (2.6 V) are also significantly higher than those of YVO_4 (1.7 V) and $EuVO_4$ (1.9 V). Therefore of the four zircons evaluated with DFT, Mg-ion intercalation is predicted to be most favorable in $EuVO_4$.

4.4. DFT predicted battery electrode properties of ABO_4 zircons

The python package, pymatgen [62], was used to analyze the Mg electrode properties that can be determined from the DFT calculations generated by the insertion algorithm. Additional calculation details are included in Appendix 7.2. These properties are reported in Table 6 which includes voltage (compared to the Mg/Mg^{2+} redox couple), gravimetric capacity (based on the ABO_4 molar mass for the charged composition without Mg), and the change in volume of the material's crystal structure between the charged and discharged state. The voltage and gravimetric capacity values are plotted in Figure 11 to show the corresponding theoretical voltage profiles for zircon YVO_4, $EuVO_4$, $YCrO_4$, and $EuCrO_4$ as Mg intercalation electrodes. The gravimetric capacities of $EuVO_4$ and $YCrO_4$ are significantly lower than those of YVO_4 and $EuCrO_4$ due to their lower maximum intercalation level of $Mg_{0.5}ABO_4$. Similarly, the predicted volume changes of YVO_4 and $EuCrO_4$ are greater than $EuVO_4$ and $YCrO_4$ due to their higher maximum intercalation level of $MgABO_4$.

ABO$_4$ Zircon	Intercalation Reaction	Voltage (V vs. Mg/Mg^{2+})	Gravimetric Capacity (mAh/g)	Volume Change (%)
YVO$_4$ mp-19133	Mg + YVO$_4$ ⇔ MgYVO$_4$	1.0	263	12
EuVO$_4$ mp-22796	0.5 Mg + EuVO$_4$ ⇔ Mg$_{0.5}$EuVO$_4$	1.9	100	7
YCrO$_4$ mp-18825	0.5 Mg + YCrO$_4$ ⇔ Mg$_{0.5}$YCrO$_4$	1.9	131	6
EuCrO$_4$ mp-22586	Mg + EuCrO$_4$ ⇔ MgEuCrO$_4$	1.8	200	10

Table 6. A summary of theoretical ABO4 zircon electrode properties calculated using DFT such as voltage (compared to the Mg/Mg^{2+} redox couple), gravimetric capacity (based on the ABO$_4$ molar mass for the charged composition without Mg), and the change in volume of the material's crystal structure between the charged and discharged state.
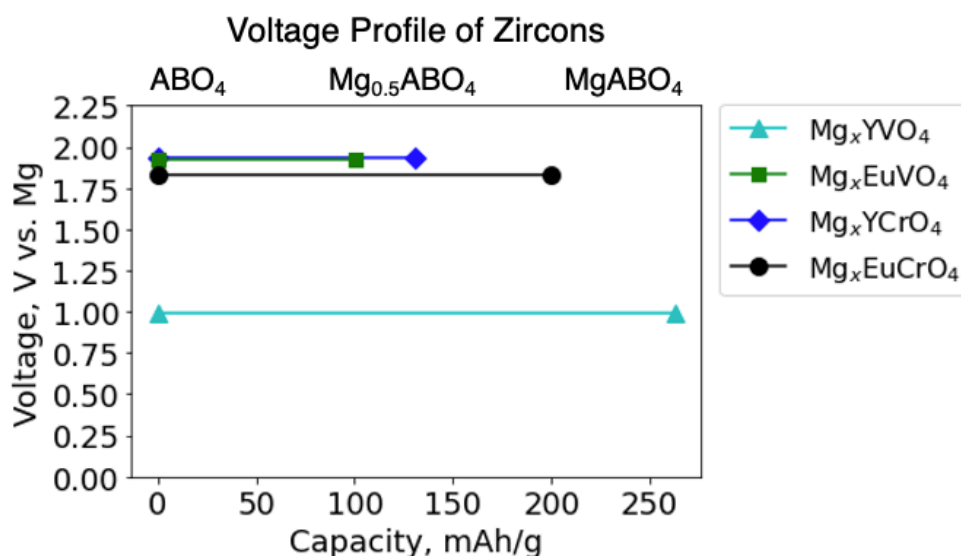

Figure 11. Theoretical voltage profiles based on DFT calculations for zircon YVO$_4$, EuVO$_4$, YCrO$_4$, and EuCrO$_4$ as Mg intercalation electrodes.

4.5. DFT predicted Mg-ion mobility of ABO$_4$ zircons

The Mg sites identified by the insertion algorithm can be used to form a migration graph mapping out a network of connected sites in the host structure [64]. This migration graph analysis enables searching for possible percolating pathways in the intercalation material. In this case, the insertion algorithm and migration graph analysis identified linear pathways consisting of the interstitial sites formed by distorted octahedra and tetrahedra. These sites form one-dimensional channels which has been previously reported in a crystallography study of the zircon structure [100]. Migration along this percolating pathway is expected to be composed of a series of repeating linear hops between interstitial sites that are approximately 1.5 Å apart. Images illustrating this pathway in a supercell of zircon YVO$_4$ are shown in Figure 12.
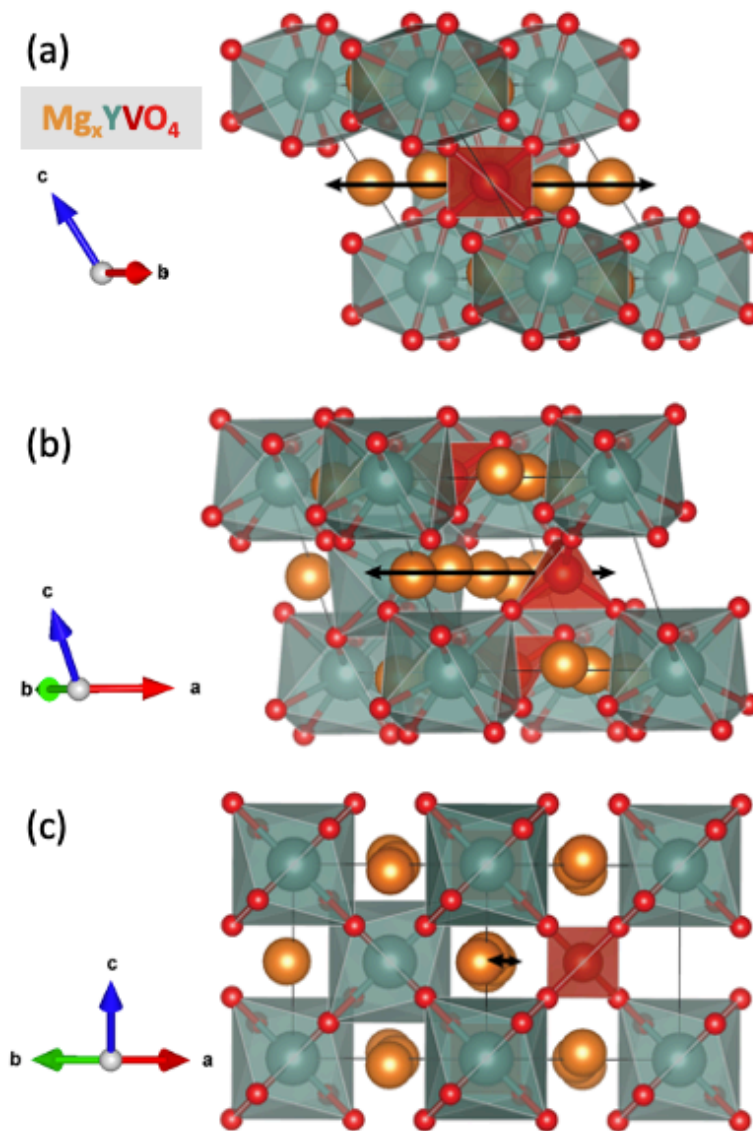
Figure 12. A YVO$_4$ zircon supercell illustrating the one-dimensional linear diffusion pathway shown from three different perspectives. In (a) the diffusion pathway is in the plane of the page while in (c), the structure is rotated 90° and the diffusion pathway is perpendicular to the plane of the page. (b) shows an intermediate perspective rotated 45° from (a) and (c).

DFT-NEB calculations were performed to evaluate the solid-state Mg-ion mobility along this path in the dilute limit of Mg ions, which in our supercell corresponds to one Mg per 16 ABO$_4$ formula units. Additional methods details are included in Appendix 7.4. The resulting change in energy as the Mg-ion traverses the linear ~1.5 Å hop in YVO$_4$, EuVO$_4$, YCrO$_4$, EuCrO$_4$ is shown in Figure 13. The Mg-ion dilute lattice limit migration barrier is 71 meV for YVO$_4$, 217 meV for EuVO$_4$, 121 meV for YCrO$_4$, and 107 for EuCrO$_4$. These migration barrier values are all remarkably low for Mg^{2+}. As a point of comparison, previous work has reported that migration barriers <650 meV would correspond to intrinsic ionic mobility sufficient for room temperature C/2 cycling with nanosized particles [19]. The dilute Mg-ion migration barrier calculated using the same methods for Chevrel Mg$_x$Mo$_6$S$_8$, the first prototype Mg cathode, is 565 meV (included in Appendix 7.1). Chevrel Mg$_x$Mo$_6$S$_8$ is the first Mg cathode experimentally

demonstrated to have sufficient rate capability for repeated cycling at room temperature [7,15]. To our knowledge, the lowest calculated Mg^{2+} migration barrier that has ever been reported is ~80 meV, for a theoretical, to date unrealized compound, $Mo_3(PO_4)_3O$ [113]. It is encouraging that high Mg-ion mobility is consistently predicted across the broader zircon family and is not limited to a specific chemistry. This suggests that these transport properties are connected to the unique structural characteristics of this family of compounds.
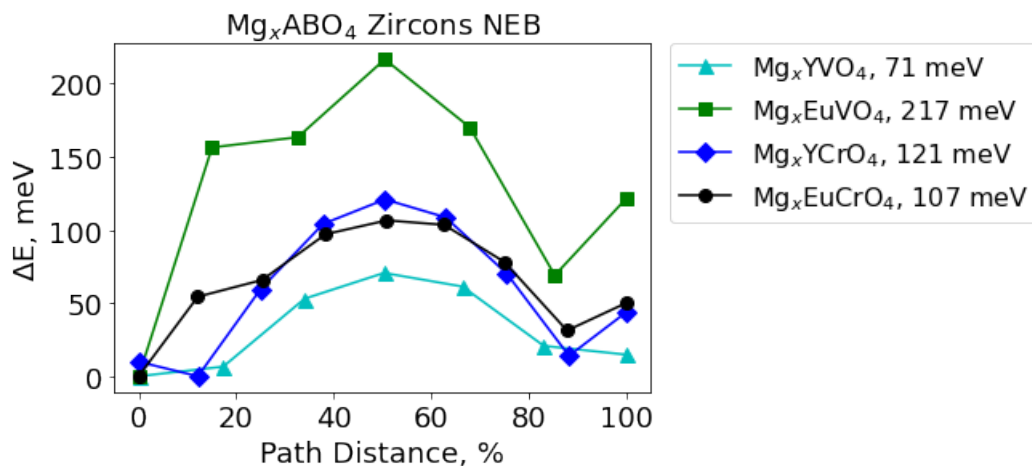

Figure 13. Energy profiles determined by DFT-NEB for Mg^{2+} migration across the characteristic ~1.5 Å linear hop at the dilute lattice limit (single Mg-ion in supercell) for zircon YVO_4, $EuVO_4$, $YCrO_4$, $EuCrO_4$.

4.6. ABO₄ zircon limitations as practical intercalation cathodes

Experimental work on several ABO_4 zircons was completed to validate these theoretical properties predicted with DFT [114]. Three zircons were successfully synthesized with nano-sized particles using a previously reported sol-gel technique [102]: YVO_4, $EuVO_4$, $EuCrO_4$. Coin cells were assembled using an activated carbon anode for electrochemical characterization and ex-situ SEM-EDS analysis to verify Mg intercalation after cycling. Overall, the best cycling performance was found for zircon $EuVO_4$ at 50°C with an initial discharge capacity of 50 mAh/g and 48 mAh/g for the 10th cycle. Zircon $EuVO_4$ had the best capacity retention compared to YVO_4 and $EuCrO_4$ which is consistent with the phase stability properties predicted by DFT. However, its experimentally measured capacity (~50 mAh/g) is still lower than expected (100 mAh/g). This initial work focused on evaluating the viability of zircon materials as Mg cathodes, but further investigations into the causes behind the limited electrochemical performance of these materials is clearly needed.

While the Mg-ion transport properties of the zircon family are attractive, this structure presents other disadvantages when considered as an intercalation cathode. The zircon structure exhibits 1-dimensional diffusion channels which usually requires nanosized primary particles in practical applications, due to the inevitable blocking of the transport passages by intrinsic anti-site defects in larger particles [115]. Indeed, initial attempts to synthesize the zircon materials by solid state methods resulted in micron sized particles, which exhibited very poor electrochemical performance [114]. Furthermore, the theoretically predicted and experimentally measured voltages are also too low to be attractive as high-performance Mg cathodes. Finally, in addition to these limitations, DFT calculations predicted poor phase stability for zircon materials upon Mg-ion intercalation, except for $EuVO_4$.

We suggest that the poor phase stability of zircon materials when discharged is connected to the reduction of the tetrahedral transition metal (B atom) in the ABO_4 zircon structure. Small, higher valence transition metals (e.g., V^{5+}, Cr^{6+}, Cr^{5+}) favor tetrahedral coordination while lower valence transition metals (e.g., V^{4+}, V^{3+}, Cr^{4+}, Cr^{3+}) favor octahedral coordination [99]. Therefore, when the redox active transition metal is reduced to a lower oxidation state upon Mg-ion intercalation ($V^{5+} \rightarrow V^{4+}$ or $Cr^{5+} \rightarrow Cr^{4+}$), the tetrahedral coordination becomes less stable. While yttrium is expected to exhibit a 3+ oxidation state, europium can be found with oxidation states of 2+ and 3+. As such, there is a possibility that Eu participates in the redox reaction upon Mg intercalation (i.e., $Eu^{3+} \rightarrow Eu^{2+}$ occurs before $V^{5+} \rightarrow V^{4+}$) which may correspond to the better capacity retention upon electrochemical cycling and predicted phase stability for $EuVO_4$.

4.7. Overlapping polyhedra structural motifs to promote multivalent ion transport

We propose that the remarkably high Mg-ion mobility predicted based on these reported NEB results is due to the unique structural motif found in ABO_4 zircon materials. As previously introduced, the zircon structure exhibits one-dimensional channels of interstitial sites composed of overlapping, distorted octahedra and tetrahedrons [100]. This one-dimensional channel in the zircon structure (see Figure 14) enables ionic transport via unusually short, repeating ~1.5 Å hops between interlocking octahedra and tetrahedra. Oxygens form a repeating pattern along the channel and can be divided into pairs of atoms (A, B, C, and D) which rotate as one moves along the migration direction which is depicted in Figure 14b and 14c. The interstitial distorted octahedral sites can be visualized by considering 3 adjacent pairs of oxygens (6 atoms total) while the tetrahedral sites are formed by 2 adjacent pairs of oxygens (4 atoms total). Figure 14d shows the two tetrahedral sites (e.g., AB and BC) contained within one distorted octahedra (e.g., ABC) which are shaded. Two neighboring distorted octahedral sites (e.g., ABC and BCD) share 4 atoms (e.g., B1, B2, C2, C2) and overlap in volume through the shared tetrahedral site (BC).

Furthermore, the distortion of the octahedral interstitial site in the zircon structure reduces the preference of a Mg-ion for this site. Minimizing the migrating ion's change in coordination along the diffusion pathway correlates with smaller site energy differences resulting in favorable, lower migration barriers because of the resulting flatter energetic landscape [19,113]. Large changes along the path to lower coordination numbers, such as 2 and 3, has been shown to correspond to the most unfavorable sites along a diffusion pathway for multivalent ions in a variety of materials [10,19,113]. This makes the zircon overlapping distorted octahedral and tetrahedral interstitial sites particularly well suited for Mg-ion transport. The interlocked interstitial sites of the 1-dimensional zircon diffusion channels result in a "6-5-4" change in coordination, which corresponds to significantly less coordination change as compared to the typical "6-3-4" change in coordination found in diffusion pathways composed of face-sharing tetrahedral and octahedral sites (see Figure 9). The intermediate coordination of 5 in the zircon structure is more much favorable than 3 because the migrating ions avoid squeezing through a plane of anions, which usually corresponds to higher energies [10].
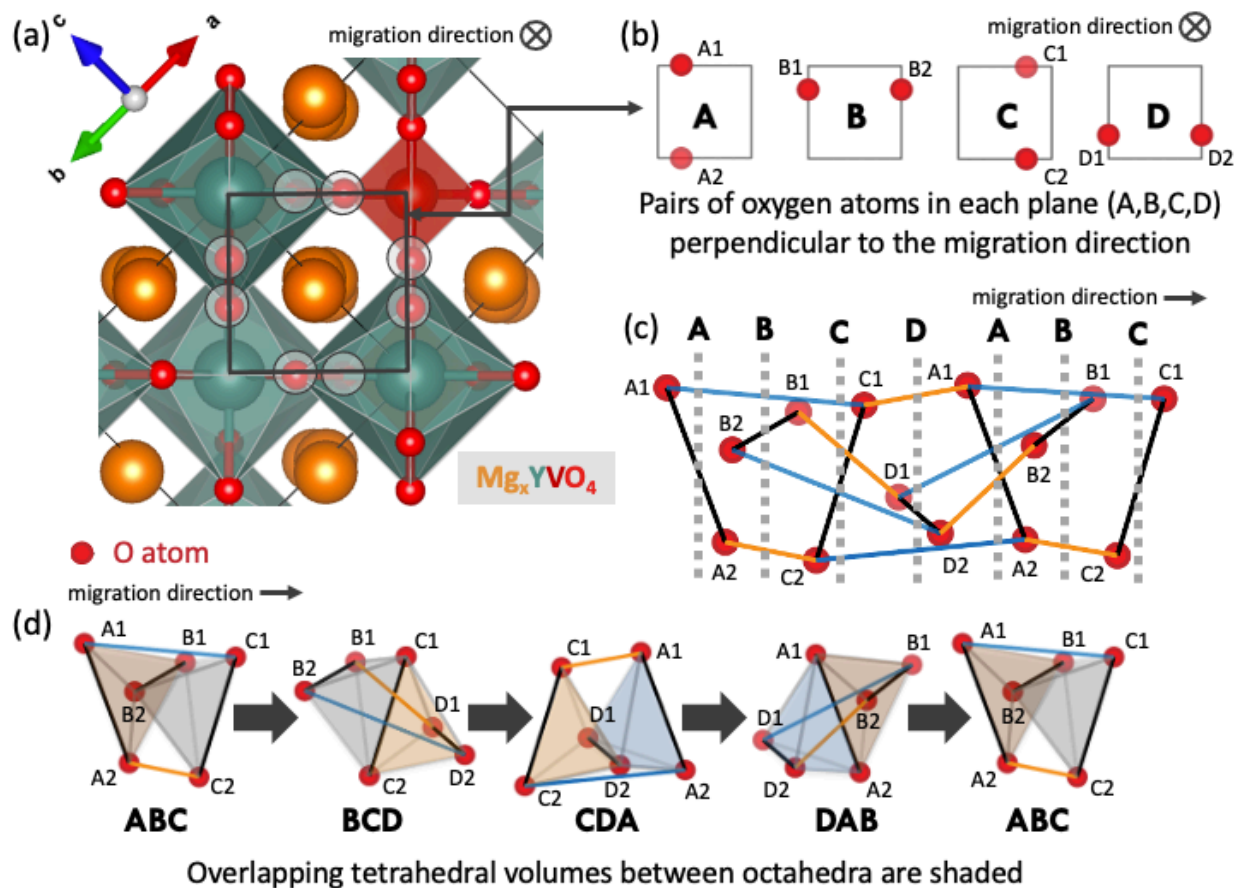
Figure 14. A depiction of the unique zircon structural motif which has one-dimensional linear channels of interstitial sites composed of distorted octahedra and tetrahedrons that are overlapping in volume.

In conclusion, this work evaluated the viability of 4 zircons (YVO_4, $EuVO_4$, $YCrO_4$, $EuCrO_4$) as Mg intercalation cathodes with DFT. Three of these materials (YVO_4, $EuVO_4$, and $EuCrO_4$) were successfully synthesized and experimentally tested to validate their electrochemical properties [114]. While all 4 zircon compounds were calculated to exhibit remarkably good Mg-ion transport with low Mg^{2+} migration barriers (<250 meV), zircon $EuVO_4$ has the best predicted phase stability and electrochemical performance upon experimental testing. We attribute the promising Mg-ion transport properties of the zircon family to their unique "6-5-4" change in coordination of the migrating ion along the diffusion pathway created by overlapping interstitial distorted octahedral and tetrahedral sites. As such, the zircon structure presents exciting design motifs for promoting Mg-ion mobility; however, the 1-dimensional diffusion pathways, limited voltages, and tetrahedral coordination of the redox-active transition metal likely limit their viability as suitable intercalation cathodes. While zircons may not serve as promising high-performance Mg cathodes, the structure family offers useful insights into material design rules based on polyhedra with overlapping volumes for improving multivalent ion transport.

5. Conclusion[5]

5.1. Significant results in searching for high-performance Mg cathodes

A novel computational materials screening framework designed to identify promising multivalent cathodes among materials that do not contain the active intercalating ion has been implemented and applied to Mg cathode discovery. The screening consists of four tiers which each focus on a different set of properties relevant for multivalent cathodes. In the first tier, all materials in the Materials Project were filtered by relative stability and composition. Then, candidate materials were filtered to include at least one reducible cation with a high enough oxidation state to permit intercalation. In the third tier, possible multivalent ion insertion sites were identified and candidates were prioritized by voltage, charge stability, and discharge stability. In the fourth and final screening tier, multivalent ion solid-state mobility is evaluated using the ApproxNEB algorithm. A major advancement in the development of this computational screening framework is the capability to evaluate the solid-state mobility of any inorganic crystalline material with automated high-throughput methods. A data set of Mg cathodes evaluated with this screening methodology, which includes complete mobility data for 85 unique structure types, has been made publicly available through MPContribs hosted by the Materials Project [56,57].

Preliminary work with this screening approach to identify high-performance Mg cathodes focused on four materials: NASICON $V_2(PO_4)_3$ (mp-26962), birnessite $NaMn_4O_8$ (mp-1016155), tavorite $MnPO_4F$ (mp-25426), and spinel MnO_2 (mp-25275). Despite having similar changes in coordination along the diffusion pathway (composed of face-sharing tetrahedrals and octahredals), the lower migration barrier of birnessite $NaMn_4O_8$ compared to spinel MnO_2 points to larger Mg^{2+} site volume as a possible characteristic for improved solid-state mobility. However, local energy maxima along the diffusion pathway did not correspond to sites of lowest volume as volume comparisons between sites of different geometries (or different local bonding environments) appear less meaningful. Instead, these local energy maxima correlated with points of lower coordination where the working ion passes through a plane of anions. A larger site volume at these lower coordination points likely reduces the observed energy penalty due to weaker Coulombic interactions with the host lattice given the larger distance from the mobile ion. Therefore, the available free volume for a given type of local bonding environment of a mobile ion site in the host structure was proposed as another influential factor for improving solid-state mobility.

The preliminary results in developing this novel computational screening approach yielded several new Mg cathode material candidates with promising energy density or solid-state mobility properties. Further computational investigation and experimental verification was pursued based on two candidates: ε-VOPO$_4$ and zircon EuCrO$_4$. ε-Mg$_x$VOPO$_4$ had attractive energy density properties with a theoretical voltage of 2.7 V vs. Mg/Mg^{2+} and gravimetric capacity of 331 mAh/g. Experimental characterization verified Mg intercalation in ε-VOPO$_4$, found an average voltage of -0.1 V vs. activated carbon (~2.3V vs Mg^{2+}/Mg), and an initial capacity of 90 mAh/g [97]. These energy density properties are a significant improvement compared to the original Mg cathode, Chevrel Mg$_x$Mo$_6$S$_8$. The low migration barrier estimated

---

[5] Portions of this chapter are adapted from References [10,114].

for zircon $EuCrO_4$ raised interest in ABO_4 (A = Y, Eu and B = V, Cr) zircons as Mg intercalation cathodes. Zircon YVO_4, $EuVO_4$, and $EuCrO_4$ were experimentally investigated and Mg intercalation was verified [114]. Of the three zircons experimentally evaluated, $EuVO_4$ exhibited the most stable and reversible electrochemical performance. These two cases validate the viability of this computational screening approach to predict novel multivalent cathodes among materials that do not already contain the working ion of interest, however there are limitations with this methodology.

The promising transport properties identified using this screening approach led to further investigation of ABO_4 (A = Y, Eu and B = V, Cr) zircons as Mg intercalation cathodes. In addition to experimental investigation, four zircons (YVO_4, $EuVO_4$, $YCrO_4$, $EuCrO_4$) were evaluated with DFT which found promising Mg^{2+} mobility (migration barriers <250 meV predicted by NEB) across multiple chemistries in this structural family. The promising Mg-ion transport properties of the zircon family were attributed to their unique "6-5-4" change in coordination of the migrating ion along the diffusion pathway created by overlapping interstitial distorted octahedral and tetrahedral sites. However, there are several drawbacks to the zircon structure that were not considering by the screening approach, such as their 1-dimensional diffusion pathways and unfavorable tetrahedral coordination of the redox-active transition metal in the structure, which limit their viability as cathodes. While zircons may not serve as promising high-performance Mg cathodes, the structure family offers useful insights into material design rules based on structural motifs containing polyhedra with overlapping volumes for improving multivalent ion transport.

5.2. Limitations and avenues for future work

While a significant advancement of the described cathode computational screening approach is the ability to estimate migration barriers in any inorganic crystalline material with automated high-throughput methods, intrinsic lattice mobility alone is not sufficient to accurately assessing transport properties. Mobile ion hopping in a host framework is a necessary and fundamental requirement for good solid-state mobility, however transport properties at larger than Angstroms length scales (e.g., nanometers, microns) are also important. There are a number of effects which are not accounted for by the ApproxNEB workflow in the screening tier focused on solid-state mobility such as the dimensionality of diffusion pathways, ordering, defects, cooperative motion, etc. The application of the ApproxNEB workflow here is also limited to the dilute lattice concentration and higher working ion concentrations are not considered. As computational cathode screenings continue to progress, ionic mobility can be better evaluated with the development and incorporation of methods that characterize transport properties at multiple length scales and various concentrations.

A motivation for this work was developing a computational screening approach suitable for cathodes that did not already contain the working ion of interest. Therefore, the second tier of the screening focused on filtering materials based on those which contained a redox active species with a high enough oxidation state that it can be reduced upon intercalation. Examining the ABO_4 zircon structure, where the transition metal is in the tetragonally coordinated B site, underscores how transition metal coordination can influence phase stability upon intercalation. When searching for cathodes in the charged state, where the oxidation state of the transition metal is higher, host materials where the transition metal is tetragonally coordinated are more

likely given the coordination preferences of transition metals based on their oxidation state. However, this tetragonal coordination is unfavorable upon reduction given the shift in preference of transition metals from tetrahedral to octahedral coordination when their oxidation state is lowered [99]. Therefore, a host material where the reducible species is in a favorable bonding environment for multiple oxidation states may have better phase stability properties upon intercalation (e.g., having V or Cr in an octahedral site). Prioritizing materials based on the preferred bonding environment of the reducible species could be a useful low-cost filtering metric for future cathode screenings.

The remarkable transport properties of the zircon family are a breakthrough finding given the difficulties in finding oxides with good multivalent ion mobility. Reducing energy penalties by avoiding unfavorable large changes in coordination along the diffusion pathway through structural motifs of polyhedra with overlapping volumes is an exciting concept for improving multivalent ion transport. Further work into developing tools for identifying these types of structural features could lead to the discovery of additional materials with promising transport properties. While the most successful magnesium cathodes reviewed in the introduction were sulfides which suffered from low voltages, this is a potential avenue for future work that could enable oxides as high-performance magnesium cathodes with both high voltages and good solid-state mobility properties.

6. Bibliography

[1]   T. Placke, R. Kloepsch, S. Dühnen, and M. Winter, *Lithium Ion, Lithium Metal, and Alternative Rechargeable Battery Technologies: The Odyssey for High Energy Density*, Journal of Solid State Electrochemistry **21**, 1939 (2017) https://doi.org/10.1007/s10008-017-3610-7.

[2]   A. Ponrouch, J. Bitenc, R. Dominko, N. Lindahl, P. Johansson, and M. R. Palacin, *Multivalent Rechargeable Batteries*, Energy Storage Mater **20**, 253 (2019) https://doi.org/10.1016/j.ensm.2019.04.012.

[3]   Y. Liang, H. Dong, D. Aurbach, and Y. Yao, *Current Status and Future Directions of Multivalent Metal-Ion Batteries*, Nat Energy **5**, 646 (2020) https://doi.org/10.1038/s41560-020-0655-0.

[4]   R. Yang, W. Yao, B. Tang, F. Zhang, X. Lei, C.-S. Lee, and Y. Tang, *Development and Challenges of Electrode Materials for Rechargeable Mg Batteries*, Energy Storage Mater **42**, 687 (2021) https://doi.org/10.1016/J.ENSM.2021.08.019.

[5]   Y. Tian et al., *Promises and Challenges of Next-Generation "Beyond Li-Ion" Batteries for Electric Vehicles and Grid Decarbonization*, Chem Rev **121**, 1623 (2021) https://doi.org/10.1021/acs.chemrev.0c00767.

[6]   G. Crabtree, *The Coming Electric Vehicle Transformation: A Future Electric Transportation Market Will Depend on Battery Innovation*, Science https://doi.org/10.1126/science.aax0704.

[7]   D. Aurbach, Z. Lu, A. Schechter, Y. Gofer, H. Gizbar, R. Turgeman, Y. Cohen, M. Moshkovich, and E. Levi, *Prototype Systems for Rechargeable Magnesium Batteries*, Nature **407**, 724 (2000) https://doi.org/10.1038/35037553.

[8]   P. Canepa, G. Sai Gautam, D. C. Hannah, R. Malik, M. Liu, K. G. Gallagher, K. A. Persson, and G. Ceder, *Odyssey of Multivalent Cathode Materials: Open Questions and Future Challenges*, Chem Rev **117**, 4287 (2017) https://doi.org/10.1021/acs.chemrev.6b00614.

[9]   Z. Rong, R. Malik, P. Canepa, G. Sai Gautam, M. Liu, A. Jain, K. Persson, and G. Ceder, *Materials Design Rules for Multivalent Ion Mobility in Intercalation Structures*, Chemistry of Materials **27**, 6016 (2015) https://doi.org/10.1021/acs.chemmater.5b02342.

[10]   A. Rutt, J.-X. Shen, M. Horton, J. Kim, J. Lin, and K. A. Persson, *Expanding the Material Search Space for Multivalent Cathodes*, ACS Appl Mater Interfaces **14**, 44367 (2022) https://doi.org/10.1021/acsami.2c11733.

[11]   M. Mao, T. Gao, S. Hou, and C. Wang, *A Critical Review of Cathodes for Rechargeable Mg Batteries*, Chem Soc Rev **47**, 8804 (2018) https://doi.org/10.1039/c8cs00319j.

[12]   A. Emly and A. Van der Ven, *Mg Intercalation in Layered and Spinel Host Crystal Structures for Mg Batteries*, Inorg Chem **54**, 4394 (2015) https://doi.org/10.1021/acs.inorgchem.5b00188.

[13]   X. Sun, P. Bonnick, V. Duffort, M. Liu, Z. Rong, K. A. Persson, G. Ceder, and L. F. Nazar, *A High Capacity Thiospinel Cathode for Mg Batteries*, Energy Environ Sci **9**, 2273 (2016) https://doi.org/10.1039/C6EE00724D.

[14]   X. Sun, P. Bonnick, and L. F. Nazar, *Layered TiS2 Positive Electrode for Mg Batteries*, ACS Energy Lett **1**, 297 (2016) https://doi.org/10.1021/acsenergylett.6b00145.

[15]   D. Aurbach, G. S. Suresh, E. Levi, A. Mitelman, O. Mizrahi, O. Chusid, and M. Brunelli, *Progress in Rechargeable Magnesium Battery Technology*, Advanced Materials **19**, 4260 (2007) https://doi.org/10.1002/adma.200701495.

[16]   N. Nitta, F. Wu, J. T. Lee, and G. Yushin, *Li-Ion Battery Materials: Present and Future*, Materials Today **18**, 252 (2015) https://doi.org/10.1016/j.mattod.2014.10.040.

[17]   M. Smeu, M. S. Hossain, Z. Wang, V. Timoshevskii, K. H. Bevan, and K. Zaghib, *Theoretical Investigation of Chevrel Phase Materials for Cathodes Accommodating Ca2+ Ions*, J Power Sources **306**, 431 (2016) https://doi.org/10.1016/j.jpowsour.2015.12.009.

[18]   M. Liu, A. Jain, Z. Rong, X. Qu, P. Canepa, R. Malik, G. Ceder, and K. A. Persson, *Evaluation of Sulfur Spinel Compounds for Multivalent Battery Cathode Applications*, Energy Environ Sci **9**, 3201 (2016) https://doi.org/10.1039/C6EE01731B.

[19]   Z. Rong, R. Malik, P. Canepa, G. Sai Gautam, M. Liu, A. Jain, K. Persson, and G. Ceder, *Materials Design Rules for Multivalent Ion Mobility in Intercalation Structures*, Chemistry of Materials **27**, 6016 (2015) https://doi.org/10.1021/acs.chemmater.5b02342.

[20]   D. Aurbach, Z. Lu, A. Schechter, Y. Gofer, H. Gizbar, R. Turgeman, Y. Cohen, M. Moshkovich, and E. Levi, *Prototype Systems for Rechargeable Magnesium Batteries*, Nature **407**, 724 (2000) https://doi.org/10.1038/35037553.

[21]   P. Canepa, G. Sai Gautam, D. C. Hannah, R. Malik, M. Liu, K. G. Gallagher, K. A. Persson, and G. Ceder, *Odyssey of Multivalent Cathode Materials: Open Questions and Future Challenges*, Chem Rev **117**, 4287 (2017) https://doi.org/10.1021/acs.chemrev.6b00614.

[22]   D. Aurbach, G. S. Suresh, E. Levi, A. Mitelman, O. Mizrahi, O. Chusid, and M. Brunelli, *Progress in Rechargeable Magnesium Battery Technology*, Advanced Materials **19**, 4260 (2007) https://doi.org/10.1002/adma.200701495.

[23]   E. Levi, E. Lancry, A. Mitelman, D. Aurbach, O. Isnard, and D. Djurado, *Phase Diagram of Mg Insertion into Chevrel Phases, MgxMo 6T8 (T = S, Se). 2. THe Crystal Structure of Triclinic MgMo6Se8*, Chemistry of Materials **18**, 3705 (2006) https://doi.org/10.1021/cm060715m.

[24]   E. Levi, E. Lancry, A. Mitelman, D. Aurbach, G. Ceder, D. Morgan, and O. Isnard, *Phase Diagram of Mg Insertion into Chevrel Phases, Mg XMo 6T 8 (T = S, Se). 1. Crystal Structure of the Sulfides*, Chemistry of Materials **18**, 5492 (2006) https://doi.org/10.1021/cm061656f.

[25]   M. Smeu, M. S. Hossain, Z. Wang, V. Timoshevskii, K. H. Bevan, and K. Zaghib, *Theoretical Investigation of Chevrel Phase Materials for Cathodes Accommodating Ca2+ Ions*, J Power Sources **306**, 431 (2016) https://doi.org/10.1016/j.jpowsour.2015.12.009.

[26]   X. Sun, P. Bonnick, and L. F. Nazar, *Layered TiS2 Positive Electrode for Mg Batteries*, ACS Energy Lett **1**, 297 (2016) https://doi.org/10.1021/acsenergylett.6b00145.

[27]   Y. Gu, Y. Katsura, T. Yoshino, H. Takagi, and K. Taniguchi, *Rechargeable Magnesium-Ion Battery Based on a TiSe2-Cathode with d-p Orbital Hybridized Electronic Structure*, Sci Rep **5**, 12486 (2015) https://doi.org/10.1038/srep12486.

[28]   A. Emly and A. Van Der Ven, *Mg Intercalation in Layered and Spinel Host Crystal Structures for Mg Batteries*, Inorg Chem **54**, 4394 (2015) https://doi.org/10.1021/acs.inorgchem.5b00188.

[29]   H. D. Yoo et al., *Fast Kinetics of Magnesium Monochloride Cations in Interlayer-Expanded Titanium Disulfide for Magnesium Rechargeable Batteries*, Nat Commun **8**, 339 (2017) https://doi.org/10.1038/s41467-017-00431-9.

[30]   T. R. Juran and M. Smeu, *TiSe2 Cathode for beyond Li-Ion Batteries*, J Power Sources **436**, 226813 (2019) https://doi.org/10.1016/j.jpowsour.2019.226813.

[31] M. Liu, Z. Rong, R. Malik, P. Canepa, A. Jain, G. Ceder, and K. A. Persson, *Spinel Compounds as Multivalent Battery Cathodes: A Systematic Evaluation Based on Ab Initio Calculations*, Energy Environ Sci **8**, 964 (2015) https://doi.org/10.1039/c4ee03389b.

[32] X. Sun, P. Bonnick, V. Duffort, M. Liu, Z. Rong, K. A. Persson, G. Ceder, and L. F. Nazar, *A High Capacity Thiospinel Cathode for Mg Batteries*, Energy Environ Sci **9**, 2273 (2016) https://doi.org/10.1039/c6ee00724d.

[33] P. Bonnick, X. Sun, K. C. Lau, C. Liao, and L. F. Nazar, *Monovalent versus Divalent Cation Diffusion in Thiospinel Ti2S4*, Journal of Physical Chemistry Letters **8**, 2253 (2017) https://doi.org/10.1021/acs.jpclett.7b00618.

[34] M. Liu, A. Jain, Z. Rong, X. Qu, P. Canepa, R. Malik, G. Ceder, and K. A. Persson, *Evaluation of Sulfur Spinel Compounds for Multivalent Battery Cathode Applications*, Energy Environ Sci **9**, 3201 (2016) https://doi.org/10.1039/c6ee01731b.

[35] Y. Xiao, L. J. Miara, Y. Wang, and G. Ceder, *Computational Screening of Cathode Coatings for Solid-State Batteries*, Joule **3**, 1252 (2019) https://doi.org/10.1016/j.joule.2019.02.006.

[36] Y. S. Meng and M. E. Arroyo-de Dompablo, *First Principles Computational Materials Design for Energy Storage Materials in Lithium Ion Batteries*, Energy Environ Sci **2**, 589 (2009) https://doi.org/10.1039/b901825e.

[37] A. Urban, D. H. Seo, and G. Ceder, *Computational Understanding of Li-Ion Batteries*, Npj Computational Materials 2016 2:1 **2**, 1 (2016) https://doi.org/10.1038/npjcompumats.2016.2.

[38] A. Jain, Y. Shin, and K. A. Persson, *Computational Predictions of Energy Materials Using Density Functional Theory*, Nat Rev Mater **1**, 15004 (2016) https://doi.org/10.1038/natrevmats.2015.4.

[39] G. Hautier, A. Jain, H. Chen, C. Moore, S. P. Ong, and G. Ceder, *Novel Mixed Polyanions Lithium-Ion Battery Cathode Materials Predicted by High-Throughput Ab Initio Computations*, J Mater Chem **21**, 17147 (2011) https://doi.org/10.1039/c1jm12216a.

[40] H. Chen, G. Hautier, A. Jain, C. Moore, B. Kang, R. Doe, L. Wu, Y. Zhu, Y. Tang, and G. Ceder, *Carbonophosphates: A New Family of Cathode Materials for Li-Ion Batteries Identified Computationally*, Chemistry of Materials **24**, 2009 (2012) https://doi.org/10.1021/cm203243x.

[41] M. E. Arroyo-de Dompablo, C. Krich, J. Nava-Avendaño, M. R. Palacín, and F. Bardé, *In Quest of Cathode Materials for Ca Ion Batteries: The CaMO 3 Perovskites (M = Mo, Cr, Mn, Fe, Co, and Ni)*, Physical Chemistry Chemical Physics **18**, 19966 (2016) https://doi.org/10.1039/C6CP03381D.

[42] X. Zhang, Z. Zhang, S. Yao, A. Chen, X. Zhao, and Z. Zhou, *An Effective Method to Screen Sodium-Based Layered Materials for Sodium Ion Batteries*, NPJ Comput Mater **4**, 13 (2018) https://doi.org/10.1038/s41524-018-0070-2.

[43] Z. Zhang, X. Zhang, X. Zhao, S. Yao, A. Chen, and Z. Zhou, *Computational Screening of Layered Materials for Multivalent Ion Batteries*, ACS Omega **4**, 7822 (2019) https://doi.org/10.1021/acsomega.9b00482.

[44] J. Wang, B. Ouyang, H. Kim, Y. Tian, G. Ceder, and H. Kim, *Computational and Experimental Search for Potential Polyanionic K-Ion Cathode Materials*, J Mater Chem A Mater **9**, 18564 (2021) https://doi.org/10.1039/D1TA05300K.

[45] Z. Lu, B. Zhu, B. W. B. Shires, D. O. Scanlon, and C. J. Pickard, *Ab Initio Random Structure Searching for Battery Cathode Materials*, J Chem Phys **154**, 174111 (2021) https://doi.org/10.1063/5.0049309.

[46] F. T. Bölle, N. R. Mathiesen, A. J. Nielsen, T. Vegge, J. M. Garcia-Lastra, and I. E. Castelli, *Autonomous Discovery of Materials for Intercalation Electrodes*, Batter Supercaps **3**, 488 (2020) https://doi.org/10.1002/batt.201900152.

[47] Z. Wang, J. Cai, Y. Han, T. Han, A. Chen, S. Ye, J. Liu, and J. Li, *Computational Screening of Spinel Structure Cathodes for Li-Ion Battery with Low Expansion and Rapid Ion Kinetics*, Comput Mater Sci **204**, 111187 (2022) https://doi.org/10.1016/j.commatsci.2022.111187.

[48] P. Maragakis, S. A. Andreev, Y. Brumer, D. R. Reichman, and E. Kaxiras, *Adaptive Nudged Elastic Band Approach for Transition State Calculation*, J Chem Phys **117**, 4651 (2002) https://doi.org/10.1063/1.1495401.

[49] E. L. Kolsbjerg, M. N. Groves, and B. Hammer, *An Automated Nudged Elastic Band Method*, J Chem Phys **145**, 094107 (2016) https://doi.org/10.1063/1.4961868.

[50] N. R. Mathiesen, H. Jónsson, T. Vegge, and J. M. García Lastra, *R-NEB: Accelerated Nudged Elastic Band Calculations by Use of Reflection Symmetry*, J Chem Theory Comput **15**, 3215 (2019) https://doi.org/10.1021/acs.jctc.8b01229.

[51] O.-P. Koistinen, F. B. Dagbjartsdóttir, V. Ásgeirsson, A. Vehtari, and H. Jónsson, *Nudged Elastic Band Calculations Accelerated with Gaussian Process Regression*, J Chem Phys **147**, 152720 (2017) https://doi.org/10.1063/1.4986787.

[52] J. A. Garrido Torres, P. C. Jennings, M. H. Hansen, J. R. Boes, and T. Bligaard, *Low-Scaling Algorithm for Nudged Elastic Band Calculations Using a Surrogate Machine Learning Model*, Phys Rev Lett **122**, 156001 (2019) https://doi.org/10.1103/PhysRevLett.122.156001.

[53] O.-P. Koistinen, V. Ásgeirsson, A. Vehtari, and H. Jónsson, *Nudged Elastic Band Calculations Accelerated with Gaussian Process Regression Based on Inverse Interatomic Distances*, J Chem Theory Comput **15**, 6738 (2019) https://doi.org/10.1021/acs.jctc.9b00692.

[54] Z. Rong, D. Kitchaev, P. Canepa, W. Huang, and G. Ceder, *An Efficient Algorithm for Finding the Minimum Energy Path for Cation Migration in Ionic Materials*, J Chem Phys **145**, 074112 (2016) https://doi.org/10.1063/1.4960790.

[55] J. Shen, M. Horton, and K. A. Persson, *A Charge-Density-Based General Cation Insertion Algorithm for Generating New Li-Ion Cathode Materials*, NPJ Comput Mater **6**, 161 (2020) https://doi.org/10.1038/s41524-020-00422-3.

[56] D. Gunter, S. Cholia, A. Jain, M. Kocher, K. Persson, L. Ramakrishnan, S. P. Ong, and G. Ceder, *Community Accessible Datastore of High-Throughput Calculations: Experiences from the Materials Project*, in *2012 SC Companion: High Performance Computing, Networking Storage and Analysis* (IEEE, 2012), pp. 1244–1251 https://doi.org/10.1109/SC.Companion.2012.150.

[57] A. Jain et al., *The Materials Project: Accelerating Materials Design Through Theory-Driven Data and Tools*, in *Handbook of Materials Modeling* (Springer International Publishing, Cham, 2018), pp. 1–34 https://doi.org/10.1007/978-3-319-42913-7_60-1.

[58] G. Hautier, S. P. Ong, A. Jain, C. J. Moore, and G. Ceder, *Accuracy of Density Functional Theory in Predicting Formation Energies of Ternary Oxides from Binary Oxides and Its*

Implication on Phase Stability, Phys Rev B **85**, 155208 (2012) https://doi.org/10.1103/PhysRevB.85.155208.

[59] S. P. Ong, L. Wang, B. Kang, and G. Ceder, *Li−Fe−P−O2 Phase Diagram from First Principles Calculations*, Chemistry of Materials **20**, 1798 (2008) https://doi.org/10.1021/cm702327g.

[60] W. Sun, S. T. Dacek, S. P. Ong, G. Hautier, A. Jain, W. D. Richards, A. C. Gamst, K. A. Persson, and G. Ceder, *The Thermodynamic Scale of Inorganic Crystalline Metastability*, Sci Adv **2**, (2016) https://doi.org/10.1126/sciadv.1600225.

[61] M. Aykol, S. S. Dwaraknath, W. Sun, and K. A. Persson, *Thermodynamic Limit for Synthesis of Metastable Inorganic Materials*, Sci Adv **4**, (2018) https://doi.org/10.1126/sciadv.aaq0148.

[62] S. P. Ong, W. D. Richards, A. Jain, G. Hautier, M. Kocher, S. Cholia, D. Gunter, V. L. Chevrier, K. A. Persson, and G. Ceder, *Python Materials Genomics (Pymatgen): A Robust, Open-Source Python Library for Materials Analysis*, Comput Mater Sci **68**, 314 (2013) https://doi.org/10.1016/j.commatsci.2012.10.028.

[63] M. O'Keefe and N. E. Brese, *Atom Sizes and Bond Lengths in Molecules and Crystals*, J Am Chem Soc **113**, 3226 (1991) https://doi.org/10.1021/ja00009a002.

[64] J.-X. Shen, H. H. Li, A. C. Rutt, M. K. Horton, and K. A. Persson, *Rapid Discovery of Cathodes, Ionic Conductors and Solid-State Electrolytes through Topological Migration Analysis*, (2022) https://doi.org/https://doi.org/10.48550/arXiv.2202.0022.

[65] K. Mathew et al., *Atomate: A High-Level Interface to Generate, Execute, and Analyze Computational Materials Science Workflows*, Comput Mater Sci **139**, 140 (2017) https://doi.org/10.1016/j.commatsci.2017.07.030.

[66] A. Wang, R. Kingsbury, M. McDermott, M. Horton, A. Jain, S. P. Ong, S. Dwaraknath, and K. A. Persson, *A Framework for Quantifying Uncertainty in DFT Energy Corrections*, Sci Rep **11**, 15496 (2021) https://doi.org/10.1038/s41598-021-94550-5.

[67] Z.-D. Huang, T. Masese, Y. Orikasa, T. Mori, and K. Yamamoto, *Vanadium Phosphate as a Promising High-Voltage Magnesium Ion (de)-Intercalation Cathode Host*, RSC Adv **5**, 8598 (2015) https://doi.org/10.1039/C4RA14416C.

[68] X. Sun, V. Duffort, B. L. Mehdi, N. D. Browning, and L. F. Nazar, *Investigation of the Mechanism of Mg Insertion in Birnessite in Nonaqueous and Aqueous Rechargeable Mg-Ion Batteries*, Chemistry of Materials **28**, 534 (2016) https://doi.org/10.1021/acs.chemmater.5b03983.

[69] K. W. Nam et al., *The High Performance of Crystal Water Containing Manganese Birnessite Cathodes for Magnesium Batteries*, Nano Lett **15**, 4071 (2015) https://doi.org/10.1021/acs.nanolett.5b01109.

[70] H. Xia et al., *A Monoclinic Polymorph of Sodium Birnessite for Ultrafast and Ultrastable Sodium Ion Storage*, Nat Commun **9**, 5100 (2018) https://doi.org/10.1038/s41467-018-07595-y.

[71] Y. Zhao et al., *Stable Alkali Metal Ion Intercalation Compounds as Optimized Metal Oxide Nanowire Cathodes for Lithium Batteries*, Nano Lett **15**, 2180 (2015) https://doi.org/10.1021/acs.nanolett.5b00284.

[72] H. Liu, Y. Wang, L. Li, K. Wang, E. Hosono, and H. Zhou, *Facile Synthesis of NaV6O15 Nanorods and Its Electrochemical Behavior as Cathode Material in Rechargeable Lithium Batteries*, J Mater Chem **19**, 7885 (2009) https://doi.org/10.1039/b912906e.

[73] M. Clites and E. Pomerantseva, *Stabilization of Battery Electrodes through Chemical Pre-Intercalation of Layered Materials*, in *Low-Dimensional Materials and Devices 2016*, edited by N. P. Kobayashi, A. A. Talin, M. S. Islam, and A. V. Davydov, Vol. 9924 (SPIE, 2016), p. 992405 https://doi.org/10.1117/12.2238655.

[74] B. Jeon, J. W. Heo, J. Hyoung, H. H. Kwak, D. M. Lee, and S. T. Hong, *Reversible Calcium-Ion Insertion in NaSICON-Type NaV2(PO4)3*, Chemistry of Materials **32**, 8772 (2020) https://doi.org/10.1021/ACS.CHEMMATER.0C01112/SUPPL_FILE/CM0C01112_SI_001.PDF.

[75] S. Kim et al., *High-Voltage Phosphate Cathodes for Rechargeable Ca-Ion Batteries*, ACS Energy Lett **5**, 3203 (2020) https://doi.org/10.1021/acsenergylett.0c01663.

[76] Q. Wang, M. Zhang, C. Zhou, and Y. Chen, *Concerted Ion-Exchange Mechanism for Sodium Diffusion and Its Promotion in Na 3 V 2 (PO 4) 3 Framework*, The Journal of Physical Chemistry C **122**, 16649 (2018) https://doi.org/10.1021/acs.jpcc.8b06120.

[77] A. Mendiboure, C. Delmas, and P. Hagenmuller, *Electrochemical Intercalation and Deintercalation of NaxMnO2 Bronzes*, J Solid State Chem **57**, 323 (1985) https://doi.org/10.1016/0022-4596(85)90194-X.

[78] X. Ma, H. Chen, and G. Ceder, *Electrochemical Properties of Monoclinic NaMnO2*, J Electrochem Soc **158**, A1307 (2011).

[79] H. Pan, Y.-S. Hu, and L. Chen, *Room-Temperature Stationary Sodium-Ion Batteries for Large-Scale Electric Energy Storage*, Energy Environ Sci **6**, 2338 (2013) https://doi.org/10.1039/c3ee40847g.

[80] R. Gover, P. Burns, A. Bryan, M. Saidi, J. Swoyer, and J. Barker, *LiVPO4F: A New Active Material for Safe Lithium-Ion Batteries*, Solid State Ion **177**, 2635 (2006) https://doi.org/10.1016/j.ssi.2006.04.049.

[81] D. Chen, G.-Q. Shao, B. Li, G.-G. Zhao, J. Li, J.-H. Liu, Z.-S. Gao, and H.-F. Zhang, *Synthesis, Crystal Structure and Electrochemical Properties of LiFePO4F Cathode Material for Li-Ion Batteries*, Electrochim Acta **147**, 663 (2014) https://doi.org/10.1016/j.electacta.2014.09.131.

[82] N. Recham, J.-N. Chotard, L. Dupont, C. Delacourt, W. Walker, M. Armand, and J.-M. Tarascon, *A 3.6 V Lithium-Based Fluorosulphate Insertion Positive Electrode for Lithium-Ion Batteries*, Nat Mater **9**, 68 (2010) https://doi.org/10.1038/nmat2590.

[83] J. Wu, G. Gao, G. Wu, B. Liu, H. Yang, X. Zhou, and J. Wang, *Tavorite-FeSO 4 F as a Potential Cathode Material for Mg Ion Batteries: A First Principles Calculation*, Phys. Chem. Chem. Phys. **16**, 22974 (2014) https://doi.org/10.1039/C4CP03176H.

[84] J. Wu, G. Gao, G. Wu, B. Liu, H. Yang, X. Zhou, and J. Wang, *MgVPO 4 F as a One-Dimensional Mg-Ion Conductor for Mg Ion Battery Positive Electrode: A First Principles Calculation*, RSC Adv. **4**, 15014 (2014) https://doi.org/10.1039/C4RA00199K.

[85] S. Dou, *Review and Prospects of Mn-Based Spinel Compounds as Cathode Materials for Lithium-Ion Batteries*, Ionics (Kiel) **21**, 3001 (2015) https://doi.org/10.1007/s11581-015-1545-5.

[86] C. Kim et al., *Direct Observation of Reversible Magnesium Ion Intercalation into a Spinel Oxide Host*, Advanced Materials **27**, 3377 (2015) https://doi.org/10.1002/adma.201500083.

[87] H. Pan, A. M. Ganose, M. Horton, M. Aykol, K. A. Persson, N. E. R. R. Zimmermann, and A. Jain, *Benchmarking Coordination Number Prediction Algorithms on Inorganic*

Crystal Structures, Inorg Chem **60**, 1590 (2021)
https://doi.org/10.1021/acs.inorgchem.0c02996.

[88] M. O'Keeffe, *A Proposed Rigorous Definition of Coordination Number*, Acta Crystallogr A **35**, 772 (1979) https://doi.org/10.1107/S0567739479001765.

[89] C. B. Barber, D. P. Dobkin, and H. Huhdanpaa, *The Quickhull Algorithm for Convex Hulls*, ACM Transactions on Mathematical Software **22**, 469 (1996) https://doi.org/10.1145/235815.235821.

[90] P. Canepa, S.-H. Bo, G. Sai Gautam, B. Key, W. D. Richards, T. Shi, Y. Tian, Y. Wang, J. Li, and G. Ceder, *High Magnesium Mobility in Ternary Spinel Chalcogenides*, Nat Commun **8**, 1759 (2017) https://doi.org/10.1038/s41467-017-01772-1.

[91] Y. C. Lin, M. F. V. Hidalgo, I. H. Chu, N. A. Chernova, M. Stanley Whittingham, and S. P. Ong, *Comparison of the Polymorphs of VOPO4 as Multi-Electron Cathodes for Rechargeable Alkali-Ion Batteries*, J Mater Chem A Mater **5**, 17421 (2017) https://doi.org/10.1039/C7TA04558A.

[92] N. A. Chernova et al., *Vanadyl Phosphates AxVOPO4 (A = Li, Na, K) as Multielectron Cathodes for Alkali-Ion Batteries*, Adv Energy Mater **10**, 1 (2020) https://doi.org/10.1002/aenm.202002638.

[93] C. Ling, R. Zhang, and F. Mizuno, *Phase Stability and Its Impact on the Electrochemical Performance of VOPO4 and LiVOPO4*, J Mater Chem A Mater **2**, 12330 (2014) https://doi.org/10.1039/c4ta01708k.

[94] X. Ji, J. Chen, F. Wang, W. Sun, Y. Ruan, L. Miao, J. Jiang, and C. Wang, *Water-Activated VOPO4 for Magnesium Ion Batteries*, Nano Lett **18**, 6441 (2018) https://doi.org/10.1021/acs.nanolett.8b02854.

[95] L. Zhou, Q. Liu, Z. Zhang, K. Zhang, F. Xiong, S. Tan, Q. An, Y. M. Kang, Z. Zhou, and L. Mai, *Interlayer-Spacing-Regulated VOPO4 Nanosheets with Fast Kinetics for High-Capacity and Durable Rechargeable Magnesium Batteries*, Advanced Materials **30**, 1801984 (2018) https://doi.org/10.1002/ADMA.201801984.

[96] Y. C. Lin et al., *Thermodynamics, Kinetics and Structural Evolution of ε-LiVOPO4 over Multiple Lithium Intercalation*, Chemistry of Materials **28**, 1794 (2016) https://doi.org/10.1021/ACS.CHEMMATER.5B04880/ASSET/IMAGES/LARGE/CM-2015-04880D_0015.JPEG.

[97] D. Sari, A. Rutt, J. Kim, Q. Chen, H. Kim, P. Kristin A., and G. Ceder, *Alkali Ion Assisted Activation of ε-VOPO4 as a Cathode Material for Mg-Ion Batteries*, (n.d.).

[98] I. D. Brown, *What Factors Determine Cation Coordination Numbers?*, Acta Crystallogr B **44**, 545 (1988) https://doi.org/10.1107/S0108768188007712.

[99] D. Waroquiers et al., *Statistical Analysis of Coordination Environments in Oxides*, Chemistry of Materials **29**, 8346 (2017) https://doi.org/10.1021/acs.chemmater.7b02766.

[100] R. J. Finch and J. M. Hanchar, *Structure and Chemistry of Zircon and Zircon-Group Minerals*, Rev Mineral Geochem **53**, 1 (2003) https://doi.org/10.2113/0530001.

[101] Y. W. Long, L. X. Yang, Y. Yu, F. Y. Li, R. C. Yu, and C. Q. Jin, *Synthesis, Structure, Magnetism and Specific Heat of YCrO4 and Its Zircon-to-Scheelite Phase Transition*, Phys Rev B Condens Matter Mater Phys **75**, 104402 (2007) https://doi.org/10.1103/PHYSREVB.75.104402/FIGURES/8/MEDIUM.

[102] R. Gangadharachar and G. T. Chandrappa, *Solution Combustion Synthesis of YVO4 Nanopowder Using V2O5.NH2O Gel: Photodegradation Studies*,

Https://Doi.Org/10.1080/0371750X.2020.1864664 **80**, 47 (2021)
https://doi.org/10.1080/0371750X.2020.1864664.

[103] Z. Huang, L. Zhang, and W. Pan, *Synthesis, Structure, Elastic Properties, Lattice Dynamics and Thermodynamics of YVO4 Polymorphs from Experiments and Density Functional Theory Calculation*, J Alloys Compd **580**, 544 (2013) https://doi.org/10.1016/J.JALLCOM.2013.07.031.

[104] Z. Huang, J. Feng, and W. Pan, *Theoretical Investigations of the Physical Properties of Zircon-Type YVO4*, J Solid State Chem **185**, 42 (2012) https://doi.org/10.1016/J.JSSC.2011.10.050.

[105] D. Errandonea, R. Lacomba-Perales, J. Ruiz-Fuertes, A. Segura, S. N. Achary, and A. K. Tyagi, *High-Pressure Structural Investigation of Several Zircon-Type Orthovanadates*, Phys Rev B Condens Matter Mater Phys **79**, 184104 (2009) https://doi.org/10.1103/PHYSREVB.79.184104/FIGURES/11/MEDIUM.

[106] L.-P. Li, G.-S. Li, Y.-F. Xue, and H. Inomata, *Structure, Luminescence, and Transport Properties of EuVO4*, J Electrochem Soc **148**, J45 (2001) https://doi.org/10.1149/1.1388633/XML.

[107] D. Ranaut and K. Mukherjee, *Van Vleck Paramagnetism and Enhancement of Effective Moment with Magnetic Field in Rare Earth Orthovanadate EuVO4*, Phys Lett A **465**, 128710 (2023) https://doi.org/10.1016/J.PHYSLETA.2023.128710.

[108] D. Errandonea, R. Kumar, J. López-Solano, P. Rodríguez-Hernández, A. Muñoz, M. G. Rabie, and R. Sáez Puche, *Experimental and Theoretical Study of Structural Properties and Phase Transitions in YAsO4 and YCrO4*, Phys Rev B Condens Matter Mater Phys **83**, 134109 (2011) https://doi.org/10.1103/PHYSREVB.83.134109/FIGURES/12/MEDIUM.

[109] H. Konno, Y. Aoki, Z. Klencsár, A. Vértes, M. Wakeshima, K. Tezuka, and Y. Hinatsu, *Structure of EuCrO4 and Its Electronic and Magnetic Properties*, Https://Doi.Org/10.1246/Bcsj.74.2335 **74**, 2335 (2002) https://doi.org/10.1246/BCSJ.74.2335.

[110] A. Morales-Sánchez, F. Fernández, and R. Sáez-Puche, *Magnetic Properties of Rare Earth Chromates RCrO4 (R=Nd, Sm and Eu)*, J Alloys Compd **201**, 161 (1993) https://doi.org/10.1016/0925-8388(93)90878-Q.

[111] T. Esaka, Y. Kobayashi, H. Obata, and H. Iwahara, *Cation Conduction in Zircon-Type Solid Solution Based on YPO4*, Solid State Ion **34**, 287 (1989) https://doi.org/10.1016/0167-2738(89)90457-8.

[112] K. Amezawa, Y. Tomii, and N. Yamamoto, *High Temperature Protonic Conduction in Ca-Doped YPO4*, Solid State Ion **162–163**, 175 (2003) https://doi.org/10.1016/S0167-2738(03)00223-6.

[113] Z. Rong, P. Xiao, M. Liu, W. Huang, D. C. Hannah, W. Scullin, K. A. Persson, and G. Ceder, *Fast Mg2+ Diffusion in Mo3(PO4)3O for Mg Batteries*, Chemical Communications **53**, 7998 (2017) https://doi.org/10.1039/c7cc02903a.

[114] A. Rutt, D. Sari, Q. Chen, J. Kim, G. Ceder, and K. A. Persson, (in press) *A Novel Structural Motif to Promote Mg-Ion Mobility: Investigating ABO4 Zircons as Magnesium Intercalation Cathodes*, ACS Appl Mater Interfaces (2023).

[115] R. Malik, D. Burch, M. Bazant, and G. Ceder, *Particle Size Dependence of the Ionic Diffusivity*, Nano Lett **10**, 4123 (2010) https://doi.org/10.1021/NL1023595/SUPPL_FILE/NL1023595_SI_001.PDF.

[116] L. Wang, T. Maxisch, and G. Ceder, *Oxidation Energies of Transition Metal Oxides within the GGA+U Framework*, Phys Rev B **73**, 195107 (2006) https://doi.org/10.1103/PhysRevB.73.195107.

[117] G. K. P. Dathar, D. Sheppard, K. J. Stevenson, and G. Henkelman, *Calculations of Li-Ion Diffusion in Olivine Phosphates*, Chemistry of Materials **23**, 4032 (2011) https://doi.org/10.1021/cm201604g.

[118] S. P. Ong, V. L. Chevrier, G. Hautier, A. Jain, C. Moore, S. Kim, X. Ma, and G. Ceder, *Voltage, Stability and Diffusion Barrier Differences between Sodium-Ion and Lithium-Ion Intercalation Materials*, Energy Environ Sci **4**, 3680 (2011) https://doi.org/10.1039/c1ee01782a.

[119] D. Morgan, A. Van der Ven, and G. Ceder, *Li Conductivity in LixMPO4 (M = Mn, Fe, Co, Ni) Olivine Materials*, Electrochemical and Solid-State Letters **7**, A30 (2004) https://doi.org/10.1149/1.1633511/XML.

[120] G. Henkelman and H. Jónsson, *Improved Tangent Estimate in the Nudged Elastic Band Method for Finding Minimum Energy Paths and Saddle Points*, J Chem Phys **113**, 9978 (2000) https://doi.org/10.1063/1.1323224.

7. Appendix

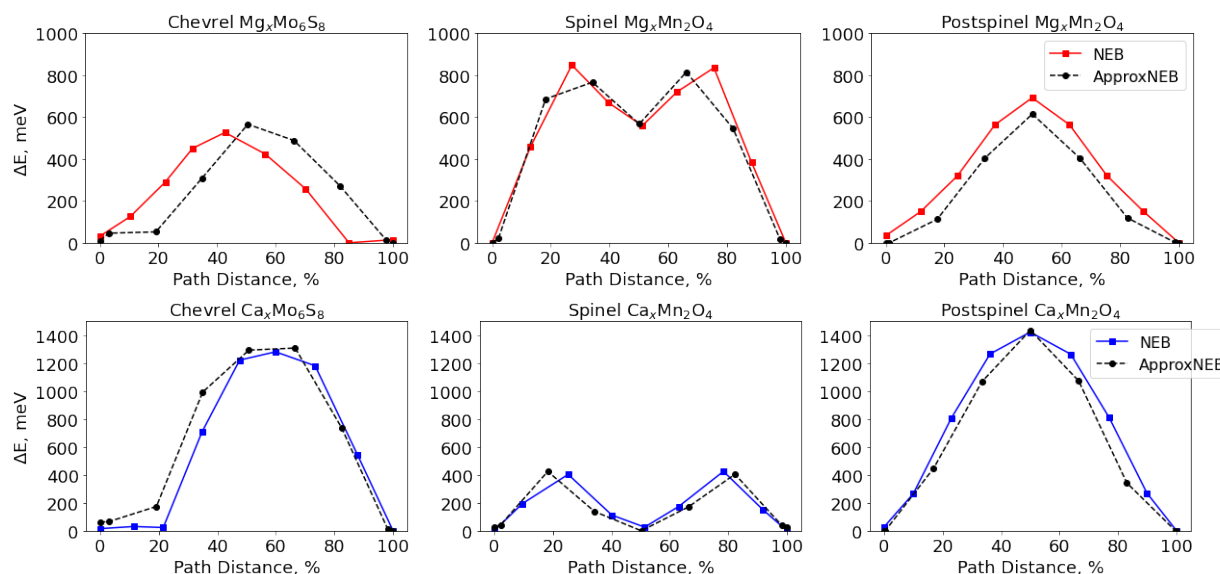## 7.1. ApproxNEB benchmarking for multivalent cathodes

Figure A.15. The results from six systems to compare ApproxNEB as a more robust and computationally alternative to NEB. Mg and Ca migration was evaluated in three known multivalent cathodes: Chevrel Mo_6S_8, spinel Mn_2O_4, and postspinel Mn_2O_4. Calculation details are in Appendix 7.3 and 7.4.

Cathode	NEB (meV)	ApproxNEB (meV)	NEB Path Distance (Å)	ApproxNEB Path Distance (Å)
Chevrel $Mg_xMo_6S_8$	527	566	6.8	6.8
Chevrel $Ca_xMo_6S_8$	1282	1309	6.9	6.5
Spinel $Mg_xMn_2O_4$	849	815	3.5	3.7
Spinel $Ca_xMn_2O_4$	425	425	3.6	3.7
Postspinel $Mg_xMn_2O_4$	692	615	2.9	3.0
Postspinel $Ca_xMn_2O_4$	1423	1436	2.9	2.9

Table A.7. Migration barriers and the corresponding path distances for the six cathode systems in Figure A.15 evaluated with both NEB and ApproxNEB.

	Computational Cost (# Nodes x Elapsed Hours)	
Cathode	NEB	ApproxNEB
Chevrel $Mg_xMo_6S_8$	306.0	11.9
Chevrel $Ca_xMo_6S_8$	489.7	16.5
Spinel $Mg_xMn_2O_4$	136.4	7.0
Spinel $Ca_xMn_2O_4$	173.9	8.3
Postspinel $Mg_xMn_2O_4$	139.3	7.4
Postspinel $Ca_xMn_2O_4$	164.5	9.9

Table A.8. A comparison of the computational cost of NEB and ApproxNEB for the 6 benchmarking systems in Figure A.15 and Table A.7 determined by the product of the number of nodes and the elapsed wall time (in hours) used in all involved calculations (e.g., end point relaxations with DFT, image relaxations with DFT, etc.)

7.2. Methods: Insertion workflow DFT calculations

Unit cell structures from the Materials Project database [56,57] are used in the "insertion algorithm" [55] which has been implemented as a workflow in the python package, Atomate [65]. The insertion algorithm uses the calculated charge density of the material to identify charge density minima which were shown to correlate strongly with viable insertion sites in known electrode materials. For each possible insertion site, the working ion of interest (such as Mg) is inserted with one working ion per unit cell and then a DFT relaxation is performed. In the high-throughput computational cathode screening, the insertion algorithm is limited a single Mg atom per unit cell structure. If further investigation into a material candidate was pursued (as for ε-VOPO$_4$ and ABO$_4$ zircons), additional Mg insertions and higher Mg concentrations were explored. If the host framework remained intact according to the structure matching capabilities in pymatgen [62] after a Mg insertion, another Mg atom was inserted into the unit cell structure according to the insertion algorithm and a DFT relaxation is performed. This process is successively repeated until either the host framework no longer remains intact, the redox capabilities of the host material is exceeded, or the energy above hull for the inserted material exceeds a given cutoff value.

DFT relaxations were performed using the Vienna Ab initio Software Package (VASP) with exchange correlation approximated with the Perdew–Burke–Ernzerhof (PBE) generalized gradient approximation (GGA). Hubbard U corrections were applied to match the Materials Project data and "MPRelaxSet" in pymatgen [62] as GGA is known for underestimating the voltage due to the incomplete cancellation of the d-orbital electrons self-interaction which can result in systematic errors when calculating redox potentials [116]. For ε-VOPO$_4$ and ABO$_4$ zircons calculations, specifically U_V = 3.25 eV and U_{Cr} = 3.7 eV were used. Pseudopotentials were also selected according to "MPRelaxSet" specified in pymatgen [62]. The total energy was sampled using a Monkhorst-Pack mesh with k-point density of 64 Å^{-3}. Projector augmented-wave theory combined with a well-converged plane-wave cutoff of 520 eV were used to describe the wave functions. The convergence threshold of the total energy was set to 0.00005 eV/atom and a force tolerance of 0.05 eV/Å.

Phase stability, which is the relative stability compared to other materials composed of the same elements, was captured by the quantity, energy per atom above the convex hull, which encloses the most stable phases within the relevant chemical space [58,59]. This "energy above hull" is 0 eV/atom for a material that is predicted to be thermodynamically stable at 0 K. Energy above hull values were calculated using phase diagrams from the Materials Project [56,57] and the MP2020 Compatibility scheme [66].

Theoretical voltages were calculated using $\Delta G_{rxn} = -nFV$, which represents the energy difference of the intercalation reaction. ΔG_{rxn} is determined using the energies from DFT produced by the insertion workflow calculations. F is Faraday's constant and n = 2 for a Mg-ion intercalation reaction.

7.3. Methods: ApproxNEB workflow DFT calculations

The ApproxNEB algorithm [54] was performed at the dilute lattice limit (single working ion in supercell) and implemented as a workflow in the python package, Atomate [65]. The Vienna Ab initio Software Package (VASP) was used to perform DFT calculations where the exchange correlation was approximated with the Perdew–Burke–Ernzerhof (PBE) generalized gradient approximation (GGA). Pseudopotentials were selected according to "MPRelaxSet" specified in pymatgen [62]. Other calculation parameters were also set to be consistent with "MPRelaxSet" unless otherwise noted. A U term was not included in these ApproxNEB calculations as there is no conclusive evidence that GGA+U performs better when investigating ion migration with methods such as NEB [31,117–119]. The total energy was sampled using a Monkhorst-Pack mesh with k-point density of 64 $Å^{-3}$. Projector augmented-wave theory combined with a well-converged plane-wave cutoff of 520 eV were used to describe the wave functions. The convergence threshold of the total energy was set to 0.0005 eV and a force tolerance of 0.05 eV/Å.

7.4. Methods: NEB and CI-NEB with DFT calculations

Nudged elastic band (NEB) calculations were performed at the dilute lattice limit to better characterize the ion mobility properties after initial ApproxNEB results. These calculations were performed using VASP with the addition of Transition State Tools for VASP software [120]. Supercells were generated to ensure lattice parameters >10 Å and avoid fictious self-interaction effects due to periodic boundary conditions.

For ε-VOPO$_4$, 2x2x2 supercells resulting in a total of 113 atoms (1 working ion per 16 VOPO$_4$ formula units) were used. For the ABO$_4$ zircons, 2x2x2 supercells were created from the unit cell structures and then transformed to orient the linear diffusion pathway and one-dimensional channels in the zircon structure along the b-axis. The migration barrier was evaluated at the dilute lattice limit where there is a single Mg atom in the host framework which resulted in supercell structures with a total of 97 atoms (one Mg per 16 ABO$_4$ formula units).

Calculation parameters consistent with "MPRelaxSet" specified in pymatgen [62] were adopted except for the following changes. A Hubbard U correction was not included in these calculations as there is no conclusive evidence that GGA+U performs better when investigating ion migration with NEB [31,117–119]. The Gaussian smearing was used. No symmetry but $\Psi_k = \Psi^*_{-k}$ was assumed to reduce sampling of the Brillouin zone. An additional support grid for the evaluation of the augmentation charge was applied. A minimum of 4 electronic self-consistency steps were required.

End point structure relaxations were converged with total energy of 0.00005 eV and force tolerance of 0.01 eV/Å cut-off criteria. A linear interpolation was used between relaxed end points. During the NEB calculation, images were converged to a total energy of 0.00005 eV and force tolerance of 0.05 eV/Å cut-off criteria. After the initial NEB calculation for ε-VOPO$_4$, the intermediate local energy minimum image was relaxed as an end point to break-up the pathway into two segments for a more refined Climbing Image NEB (CI-NEB) calculation. In CI-NEB, the images were converged to 0.00005 eV and 0.01 eV/Å.